A BOROSCOPIC QUANTITATIVE IMAGING TECHNIQUE FOR SHEET FLOW MEASUREMENTS

A Thesis

Presented to the Faculty of the Graduate School

of Cornell University

In Partial Fulfillment of the Requirements for the Degree of

Master of Science

by

Russell David Dudley

May 2007

ABSTRACT

A boroscopic imaging system is developed to measure sediment velocities within a highly concentrated sheet layer in open channel flows. A detailed literature review is presented to investigate previous attempts at sheet layer measurements, followed by a set of experiments to determine clean water flow characteristics in the open channel flume located in the DeFrees Hydraulics Laboratory. Experiments are carried out in the same flume under sediment-laden, sheet flow conditions to determine the steadiness of the flow as well as to verify velocities in the suspended sediment transport region with existing theories.

Sediment velocities are captured in the highly concentrated sediment sheet for the same flow conditions using the new boroscopic imaging system. The boroscope is a minimally intrusive lens with a diameter that is only an order of magnitude larger than the natural sand being studied. Minimum Quadratic Difference techniques, along with several filtering techniques, are utilized to determine particle displacements. A rigorous investigation into calibrations is included in order to convert pixel displacements into physical velocities. Three separate metrics are investigated, all involving light intensity values. These metrics are examined from calibrations performed under fixed, moving and in-situ experimental conditions. The limitation of each calibration as well as a discussion of the effectiveness of the calibration techniques is included.

Physical velocities within the sheet layer are determined using the in-situ variance of intensity calibration. A complete streamwise velocity profile spanning from the non-moving bed to the free stream is included which combines velocity data collected from both the boroscopic imaging technique as well as an acoustic Doppler velocimeter. The joint profile seems fairly continuous but more attention needs to be

focused on the velocities located along the interface of the sheet flow and suspended regions as well as possible reasons for differences between these experimental results and results published previously.

Finally, future development is discussed including the further investigation into calibration techniques, the possibility of measuring sediment concentrations as well as water velocities and other possible uses for the boroscopic quantitative imaging technique.

BIOGRAPHICAL SKETCH

The author was born in a small Iowa town in 1979. It was in an old aluminum canoe that he discovered both how integral water was to the environment and how often it was taken for granted. He enrolled in civil engineering at Iowa State University without really understanding anything about the major except that civil engineers spent more time outside than any of the other engineering professions. After graduating with a Bachelors of Science in Civil and Environmental Engineering, he continued his education at Cornell University pursuing a graduate degree in Environmental Fluid Mechanics and Hydrology. His time at Cornell was divided between field and laboratory research and working with students of all levels. He currently works for a private consulting firm specializing in stream restoration.

To my family and friends everywhere

ACKNOWLEDGMENTS

I remember, after my first semester at Cornell, being so tired that I couldn't sleep. This was my introduction to graduate student life at Cornell University, where my professors, my students and even the weather required my best effort day in and day out. Although there is no way to acknowledge everyone, it is important to mention several people who motivated and inspired my work at Cornell.

First and foremost, I have the utmost respect and admiration for my advisors, Professor Philip L-F. Liu and Professor Edwin A. Cowen. They are both excellent researchers and educators and have provided an incredible amount of insight and support in both of these facets during my tenure at Cornell. Their immense knowledge of fluid mechanics and passionate curiosity about environmental physics originally inspired me to study at Cornell and continues to inspire me today. I owe them both a great deal of gratitude for providing me the opportunity and support to cut my teeth in this field.

Along with my advisors, I received a great deal of help from fellow graduate students Evan Variano, Qian Liao and Yong Sung Park. All three are extremely talented in environmental fluid mechanics research and very generous of their time to help me on my project. Their knowledge and skills proved critical to my research and, when they all eventually become advisors themselves, I have no doubt they will be three of the best.

This thesis would never have been completed if not for the expert help of several talented people within Hollister Hall, namely Dr. Monroe Weber-Shirk, Tim Brock, Paul Charles, Cameron Willkens and Lee Virtue. After several hundred hours spent in the lab, I learned that things will break. Often dramatically. And often of my own doing. These were the people that fixed them and I am extremely grateful for their help.

The community of civil engineering graduate students at Cornell University is, without a doubt, vibrant and unique. I am appreciative of the help I received from everyone and am proud to be considered a peer. I am especially indebted to Chad Helmle, P.J. Rusello, Evan Variano and Brendan Lazar. You all helped keep me sane and came along when I went a little crazy. I only hope that I can repay all of your support over the course of a life-long friendship. And I would be remiss not to mention the many friends I've made throughout my life that stuck with me through this entire experience, especially my close friends Jon Fiddelke and Jeremy Bries.

Finally, if not for my family, I think I might have left after that first semester and never came back. My father, my mother, my brother and my sister are amazing people that continually astound me. My desire to contribute something positive to this world comes about because I have witnessed firsthand all of the positive things they have already contributed.

TABLE OF CONTENTS

LIST OF FIGURES

LIST OF DIAGRAMS

LIST OF IMAGES

LIST OF TABLES

LIST OF ABBREVIATIONS

SNR	Signal to Noise Ratio
ADV	Acoustic Doppler Velocimeter
MQD	Minimum Quadratic Difference
PIV	Particle Image Velocimetry
TTL	Transistor-Transistor Logic

LIST OF SYMBOLS

h	water depth
b	flume width
x	development length
T	temperature
S	channel slope
u	average velocity
z	vertical location
κ	von Kármán's constant
υ	kinematic viscosity
C	Reynold's dependent fitting parameter
Θ	physical image size
I	intensity
δ	distance from scope tip
φ	variance of intensity
ω	MQD pixel displacement
U	streamwise velocity
U_*	frictional velocity
d_{50}	median grain diameter
$\bar{u}$	average sediment velocity

CHAPTER 1

INTRODUCTION

1.1 Motivation

Nearly 53% of the population of the United States live in coastal counties, with an estimated growth of 3,600 people per day (Carlowicz 2004). Trillions of dollars have been invested in housing and infrastructure along the Atlantic and Gulf coasts alone. While the demand for coastal property increases, rising sea levels are causing shore recession at an accelerating rate. According to a recent study, beaches on the east coast of the United States are eroding at a rate of nearly 1 meter per year, putting beachfront property at risk (Leatherman 2003). Coastal erosion is not only dramatic but widespread. The same study claims nearly 90% of the U.S. sandy coasts are eroding.

The majority of sediment movement in the ocean occurs in the nearshore region, which consists of the surf zone and swash zone (Carlowicz 2004). The swash zone is defined as "the region in which the beach face is intermittently exposed to the atmosphere (Elfrink and Baldock 2002)." Because of high free stream velocities and decreasing water depths, swash zone flows are supercritical flows resulting in the sheet flow condition, which accounts for the bulk of sediment transport. Sheet flow conditions are generally present around a Froude number of 0.5 and are considered part of the upper flow regime. Sheet flow conditions lead to a plane bed surface, or a surface without any bed forms larger than the largest grain size in the bed.

Although there is an immediate need for detailed measurements within the swash zone for the development of sediment transport models, research in the swash zone has received less focus than that in the surf zone. The complexity of the swash

zone processes as well as the difficulty of measurement within the swash zone is the hindrance to the advancement of swash zone research.

The quest to accurately measure sediment velocities has led researchers to try a variety of techniques. Over the past few decades acoustic-, optical- and conductivity-based devices have been developed and modified to measure sediment-laden flow properties. Yet with these advancements in techniques, measurement of sediment velocities in the densely-concentrated sheet layer still remains both necessary and elusive.

Measurement in the high velocity, dense sediment sheet layer is complicated by the thinness of the layer, which is typically ~ 5-20 grain diameters in thickness (Sumer et al. 1996). The shallowness of the sheet layer prohibits the use of many acoustic techniques, such as acoustic Doppler velocimetry (ADV), from profiling velocities within a sheet where the thickness is on the same order as the sampling volume. Optical techniques, such as laser Doppler velocimetry (LDV) or particle image velocimetry (PIV), are in general using smaller sample volumes and are ideal for resolving sediment velocities within the thin sheet layer. However, most of the existing LDV and PIV techniques generally involve highly-sensitive equipment as well as elaborate configurations, requiring that the techniques be set-up external to the flow. The external nature of the techniques severely limits the ability to perform measurements within the high sediment concentration of the sheet.

This study proposes the use of a minimally intrusive imaging technique to capture sediment velocities within the sheet layer. A rigid, fiberoptic scope is developed as a lens to image within the sheet flow region. The scope includes two separate windows; one for imaging and the other for light delivery. The scope is an order of magnitude larger than the imaged sediment grain size and minimally affects the flow under sheet conditions. Sediment velocities are extracted by analyzing

structures within the images by means of the minimum quadratic difference (Gui and Merzkirch 2000).

1.2 Literature Review

The difficulties in measuring sediment-laden turbulent flow velocities are evident by the number of different techniques researchers and scientists have attempted in the last century. Measurement techniques have evolved to include acoustic-, optical- and even conductivity-based techniques.

Horikawa et al. (1982) measured sediment transport under sheet flow conditions using a motor-driven 35 mm camera. An oscillatory flow tank with a 200 cm test section was used for the experiments and sand transport was studied using natural sand with a median grain size of 0.2 mm. The focus of the experiment was to determine the inception of sheet flow although sediment transport rates were also measured by tracking particles within a series of images. This restricted particle velocity measurement to very near the flume side wall.

Dick and Sleath (1991) also measured sediment transport in an oscillatory flow tank yet used sediments with a mean diameter greater than natural sand and a particle density much closer to water than to natural sands. A laser-Doppler anemometer was used in backscatter mode to measure velocities. Sediment particles entering the sampling volume increased the backscatter light intensity, causing the tracker to lose the signal while the sediment particle is in the sampling volume. Dick and Sleath made the assumption that the velocity recorded was the fluid velocity only and that slippage between the sediment particles and the fluid was negligible due to the sediment density and fluid density being approximately equal.

Sumer et al. (1996) measured sediment velocities and concentrations within the sheet flow layer under steady currents. They used a variety of different particles with varying diameters and specific weights from uniformly distributed plastic spheres (diameter = 3 mm, Specific Gravity = 1.27) to natural sand (diameter = 0.13 mm, Specific Gravity = 2.65). Although they used a Conductivity Concentration Meter (CCM) probe to measure sediment concentrations within the sheet layer, a Pitot-tube with an outside diameter of 5 mm was used to measure sediment velocities. The use of a Pitot-tube limited sheet flow velocity measurements to runs with large particles, where the sheet flow layer was larger.

Fitting the logarithmic law to the measured flow velocity near the bed, but outside of the sheet layer, they compared measured values of Nikurdse's equivalent sand roughness (k_s). To fit the logarithmic law, they set the von Kármán's constant to 0.407. They noticed that velocity profile measurements resulted in a smaller values of k_s/d compared to those found from the flow resistance calculations. They hypothesized that this might have been due to the value of the von Kármán's constant used or that the logarithmic layer was relatively thin. They claimed the logarithmic-velocity layer exists mostly outside of the sheet flow layer and that the velocity profile within the sheet flow layer can be represented by a power law. They also cautioned that their measurements only covered the condition of sheet flow with no suspended sediment and that experimental constraints prevented extension to the case of sheet flow with suspended sediment.

Kaftori et al. (1995) also used laser-Doppler anemometry to study particle-laden turbulent flows. Much like Dick and Sleath, the particles used were only slightly denser than the surrounding fluid. Measurements were carried out in a recirculating flume to study the motion of particles near the smooth flume bottom at relatively low Reynolds numbers. Unlike Dick and Sleath, Kaftori et al. utilized an

amplitude discrimination technique to differentiate between the solid particle and fluid velocities. Kaftori et al. determined that coherent wall structures were primarily responsible for particle motion near a solid boundary, specifically that the behavior of the particles indicated the presence of funnel vortices. Their work focused on the intricacies of deposition and entrainment under the simplified condition of a smooth boundary.

Bennett et al. (1998) used a laser-Doppler anemometry with a discriminator technique to measure sediment and fluid velocities over both mobile and fixed beds. Sheet flow conditions were studied and although glass beads were used instead of natural sand, the density and grain size were similar to that of natural sand. Velocities were measured in the suspended region, starting at 5 mm above the local bed elevation, for the mobile bed experiments.

Muste et al. (1996) also developed a laser-Doppler anemometry technique which distinguished between sediment and fluid velocities. Claiming simple amplitude discrimination was not sufficient to resolve the two separate velocities, they added a separate system consisting of a photomultiplier and receiving optics. The combination of the laser-Doppler anemometer signal and the additional discriminator output was used to distinguish sediment and fluid velocities. Muste et al. was able to use this technique on flows containing natural sand but only at very low sediment concentrations.

Muste et al. (1997) hypothesized that the addition of sand was similar to increasing roughness, by changing the flow conditions near the bed. They noted that the shift in velocity was minor due to the low sediment concentrations used in the experiments. To achieve large changes in the velocity profile, the bed roughness would need to change dramatically. They note the importance of extending the range of sediment size and concentration in future experiments.

Laser-Doppler anemometry has the advantage of being an external technique and thus not impacting the flow. Discriminator techniques have been developed to differentiate between sediment and fluid velocities yet the use of this technique becomes unreliable in highly-concentrated flows such as found within the sheet. To measure velocities in the sheet, Dohmen-Janssen and Hanes (2002) utilized a pair of Conductivity Concentration Meters (CCMs) which were originally developed to measure sediment concentrations (see Ribberink and Al-Salem, 1995). The CCM measured the electrical conductivity of the sediment-laden fluid using four electrodes, each with a thickness of 0.3 mm and spaced 0.6 mm apart. The CCM probes were buried in the bed and could be moved up and down with a vertical positioning system. The probes were placed such that one probe was located 15 mm downstream of the other. Velocities within the sheet layer were calculated by the cross-correlation of the two concentration signals (Dohmen-Janssen and Hanes 2002).

Dohmen-Janssen and Hanes measured sheet flow dynamics produced by monochromatic breaking waves in a large wave flume. They noted that it was the first time sediment concentrations and velocities were measured within the sheet flow layer under prototype waves yet added that sediment velocities could only be determined under wave crests. Similar measurements were taken by McLean et al. (2001) for oscillatory sheet flow with a mean current, utilizing the CCM probes and cross-correlation technique to determine sediment velocities.

The ability to measure sediment velocities and concentrations within the sheet is, as McLean et al. states, "a step toward better understanding of the complex sheet flow layer." Yet they also acknowledge the possibility of error introduced by the technique. The CCM probes are intrusive instruments. To obtain velocity measurements, one probe must be placed downstream in the wake of the other. McLean et al. placed the probes 20 mm, or 5 probe diameters, apart to eliminate wake

effects. This minimizes wake effects but at a cost of a larger sampling volume. Also, the correlation procedure produces weak peak signals under sinusoidal wave conditions. Dohmen-Janssen and Hanes noted that grain velocities within the sheet flow layer could only be determined under wave crests when the sheet flow layer is thicker and the velocities are much higher. This is promising for the application of CCM probes for unidirectional sheet-flow measurements. Yet even under more ideal, unidirectional sheet flow conditions, the CCM probes are unable to determine fluid velocity within the sheet flow layer, take measurements on the boundary between moving and immobile grains or determine actual shear stress and effective drag coefficient.

The CCM measurements represent some of the most advanced velocity measurements currently available within the sheet flow layer. Dohmen-Janssen and Hanes discovered that grain velocities are relatively high within the sheet flow layer, creating sediment fluxes in the sheet that are much larger than suspended sediment fluxes. They note that the high velocities along with the high concentrations indicate that the majority of sediment transport occurs in the sheet flow layer, making the study of this region crucial to the advancement of the field of sediment transport. In conclusion, although significant advances have been made in sediment velocity measurement, there is still a need for a single point measurement of sediment velocity within the sheet flow layer.

1.3 Thesis Layout

This thesis focuses on the development of an intrusive fiberoptic measurement technique. All flow experiments are carried out in an open channel recirculating flume. Details of the flume as well as the other equipment used, along with limitations

of the equipment, are included in Chapter 2. An initial analysis of the flume characteristics under clean-water flow conditions is included to establish the validity of the flume for experimental work and is included in Chapter 3. Chapter 4 details the intricacies of the boroscope, including calibration procedures. Velocities of sediment-laden turbulent flow under sheet flow conditions, including profiles within both the sheet layer as well as the suspended region, are included in Chapter 5. Finally, a discussion of the results along with suggestions for future work is included in Chapter 6.

CHAPTER 2

EXPERIMENTAL FACILITIES AND TECHNIQUES

2.1 Experimental Method

Experiments are conducted at different flow conditions for clean water analysis and sediment-laden analysis. Clean water conditions are established to investigate the characteristics of the flume in terms of boundary layer development length. Depth and flow-rate are set to create fully developed conditions within the flume. These are not the same conditions used for sediment-laden experiments, as the fully-developed clean water conditions do not create sheet flow conditions in sediment-laden flows. The flume is simply not long enough to create fully-developed sediment-laden sheet flow. This is not a detriment as much as a reality, since fully-developed sheet flow is not necessarily required to produce quantifiable results. The conditions for clean water flows help establish the validity of the open channel flume while the sediment-laden conditions help establish the validity of the fiberoptic imaging technique. A minimum of 15 points are taken for each clean water, sediment-laden and sheet flow profile. Each point is sampled fast enough to extract spectral information and long enough to develop stable averages.

This thesis utilizes a wide variety of data collection equipment. Along with the development of a new fiberoptic measurement technique, acoustic-based equipment is used to provide flume characteristics and verify flow conditions with theory.

2.2 Flume Characteristics

All experiments are carried out in an open channel flume in the DeFrees Hydraulics Laboratory (see Image 2.1). The flume is approximately 9 m long, 0.6 m wide and 0.45 m deep. The channel is constructed of clear plastic with a steel support casing, the inlet and outlet sections are constructed of high density polyethylene. The bed slope of the flume is adjustable around a single pivot, located at the downstream end of the flume. The bed slope is adjusted by trial and error until it matches the free surface slope for the desired pump speed and water depth. To reduce entrance effects, a honeycomb grid constructed of 2' long PVC pipes (I.D. of 2") is placed vertically within the inlet section below the channel bed. A variable speed centrifugal pump is used to recirculate the flow. A storage tank of approximately 500 gallons is placed between the flume outlet and the pump in order to minimize fluctuations in pump efficiency.

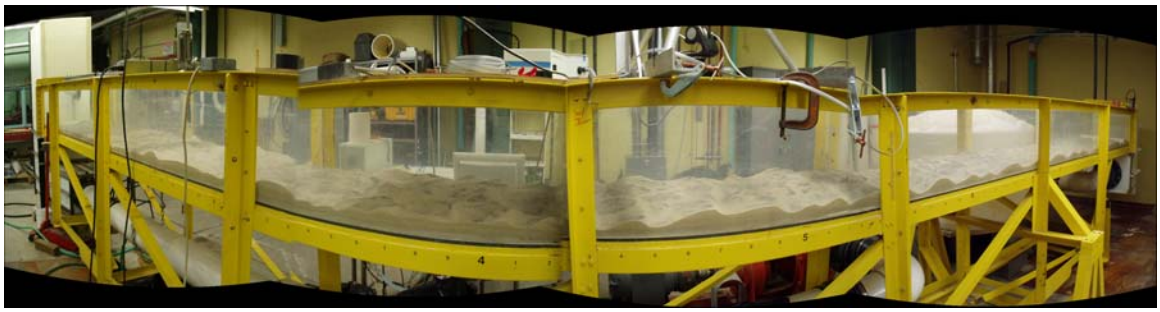

Image 2.1 DeFrees Laboratory Open Channel Sediment Recirculating Flume

The experimental test section is located approximately 6.3 m from the flume inlet. This is far enough from the inlet to eliminate entrance effects and far enough from the outlet to limit drawdown effects from the exit weir. A diagram of the flume and the measurement location is shown in Diagram 2.1.

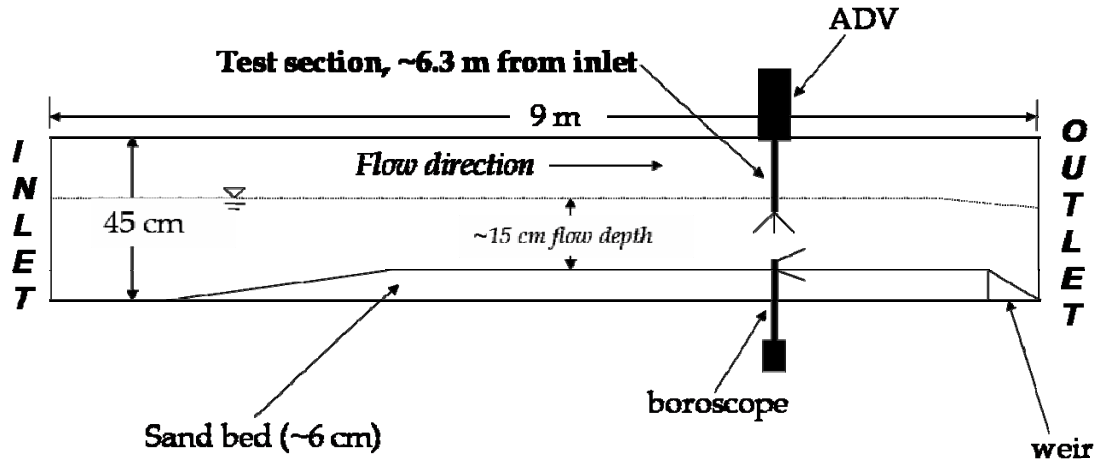

Diagram 2.1 Flume Measurements

2.3 Equipment

Along with the development of a new fiberoptic imaging technique, a variety of other data collection equipment is used to quantify flume and flow characteristics. A summary of the equipment used is detailed below.

2.3.1 Wavegages

Free surface measurements are conducted to determine the steadiness of the flow. A Banner Engineering S18U ultrasonic analog output sensor is used to measure variations in free surface elevation. The sensor consists of a central transducer that emits an ultrasonic frequency at 300 kHz and records the return pulse. The sensor features programmable maximum and minimum limits established over a 0-10 volt analog range. A range between 5 and 30 cm is selected for free surface measurements. The wave gage is mounted on the top of the flume along the flume centerline at the

test location. A schematic of the wave gage, including dimensions, is shown in Diagram 2.2.

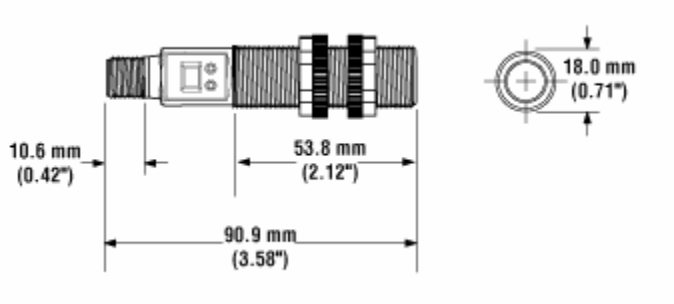

Diagram 2.2 S18U ultrasonic meter (Courtesy of Banner Engineering)

2.3.2 Acoustic Doppler Velocimeters

Two different acoustic Doppler velocimeters (ADVs) are used for velocity measurement in both clean water and sediment-laden flows. A SonTek 10 MHz ADV is utilized for velocity measurements in clean water flows. The SonTek is a coherent Doppler system consisting of a central transducer and three receiving transducers. The SonTek has a sampling volume of 0.25 cm^3, a distance to the sample volume of 5 cm and is capable of resolving velocities in three directions at a resolution of 0.01 cm/s.

A Nortek Vectrino is utilized for velocity measurements in sediment-laden flows. The Vectrino is also a coherent Doppler system with a central transducer although while the SonTek ADV has three receivers, the Nortek Vectrino includes a fourth receiver which allows redundancy in the z-direction. The distance to sample volume is 5 cm but the sample volume itself is user-specified. The transmit length as well as the power can also be adjusted and the velocity accuracy is ±0.5% of the measured value. In general, a nominal velocity range of ±1 m/s was used for the experiments.

2.3.3 Imaging System

The imaging system is mounted to the underside of the flume, as seen in Image 2.2. The boroscope and camera are attached to the vertical positioning slide along with the vertical position motor. The slide, the motor, the boroscope and the camera are attached to a solid plastic disk approximately 1" thick. This entire assembly is bolted to the underside of the flume and sealed to prevent leaks. The boroscope is guided into the sediment bed using adjustable Swagelok tube fittings on both the top and bottom of the flume bed. These fittings include small rubber gaskets which help stabilize the boroscope as well as seal the boroscope from the sand and water mixture in the flume. A description of the individual components of the system is included below.

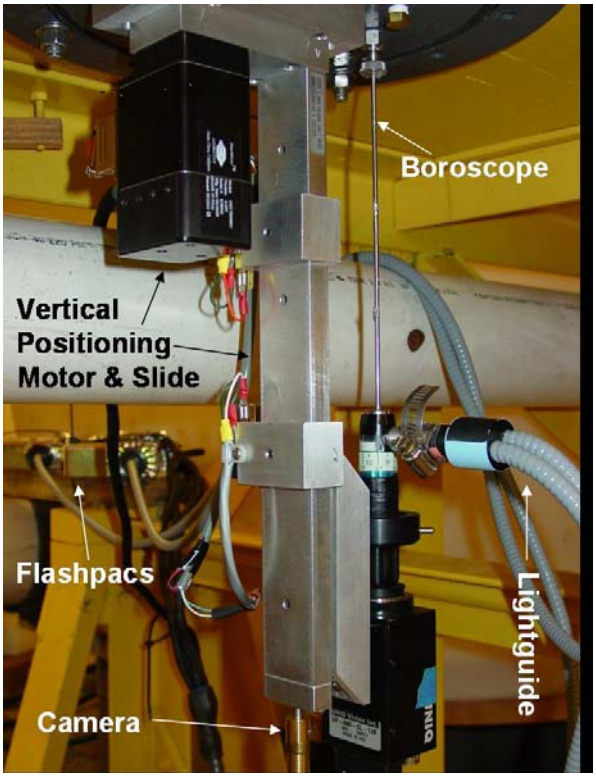

Image 2.2 Imaging System

2.3.3.1 Boroscope

Custom-made boroscopes are used for the lenses and were developed by Volpi Manufacturing USA. Each scope has an outside diameter of 2.7 mm and a length of 295 mm and includes a single optical element for image collection and separate fibers that deliver light to the distal tip. Image 2.3 displays the boroscope while Diagram 2.2 displays a sketch of the boroscope base components.

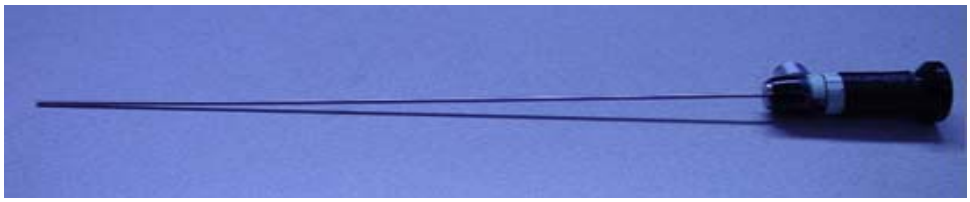

Image 2.3 Fiberoptic Boroscope

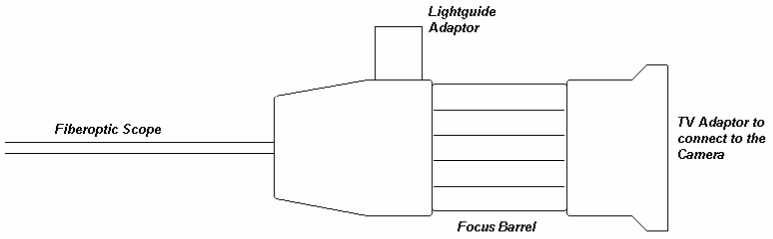

Diagram 2.3 Boroscope Base

Initial boroscope designs have an imaging window that looks straight out from the distal tip while the second generation of boroscopes includes a sealed prism so that the imaging window is located 90 degrees from the original location. While original

boroscopes have a ring of fibers that delivers light through the same opening as the image delivery system, second generation boroscopes have separate windows for light and image delivery (see Image 2.3). Each boroscope has a focus. Boroscopes are attached to the cameras with a C-mount TV adaptor which also contains a lens and focus.

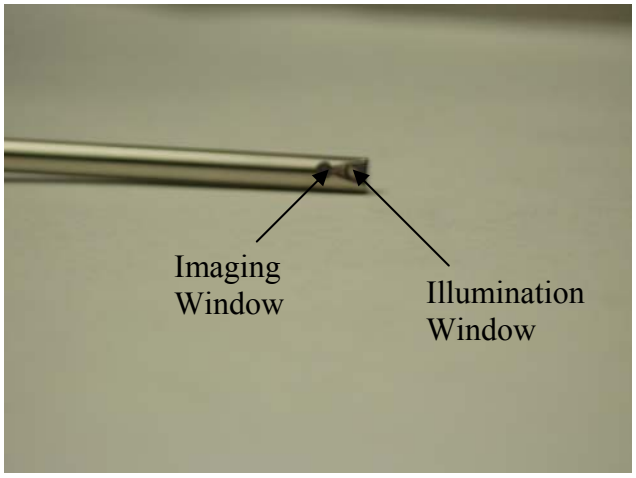

Image 2.3 Boroscope Distal Tip

2.3.3.2 Uniq CL680 Camera

A Uniq 680-CL camera is coupled with the boroscope to obtain images within the sheet flow region. The Uniq 680-CL is a monochromatic progressive scan CCD-type camera with a sensor size of 659 x 494 pixels. The Uniq camera can take images at 12 bits per pixel at speeds up to 60 fps. The Uniq camera allows for area of interest imaging, which enables the user to adjust the width and length of the image to increase frame transfer times, and also utilizes asynchronous frame capture.

The camera is triggered by the falling edge of a transistor-transistor logic (TTL) signal (this occurs when the TTL chip's voltage drops below ~0.8V with

respect to the ground terminal). A falling edge closes the shutter of the first image, transfers the image off the chip and then opens the shutter for the second image. This process takes about 20 microseconds and is the limiting factor of Δt, the time between flashes. The frame rate (defined here as the number of frames per second) is limited by the transfer of the image from the camera to the computer. The maximum bandwidth of the data acquisition system is 60 frames per second.

2.3.3.3 Flashpacs

External illumination is provided by PerkinElmer LS 1130-2 Pulsed Xenon Flashpacs (flashpacs) shown below in Image 2.4. These flashpacs are triggered by the rising edge of a TTL signal and can pulse at a maximum rate of 180 Hz. A maximum input energy of 110 mJ is available per flash. Two flashpacs are coupled with a camera and boroscope to ensure that light delivery is not dependent upon the recharge time.

Image 2.4 Flashpac

These flashpacs are coupled to the system by means of a fiberoptic light delivery guide (lightguide) that is custom made by Volpi Manufacturing USA. The lightguide is approximately one meter long, flexible, and joined together at the lightguide adaptor located on the boroscope base. The lightguide is pictured in Image 2.5 below.

Image 2.5 Lightguide

2.3.3.4 Vertical Positioning System

Movement of the boroscope vertically through the bed as well as any movement necessary for calibration is accomplished using an Animatics SM 1720 SmartMotor and an adjustment slide with a resolution of $1/1000^{th}$ of an inch. The SmartMotor requires 48 VDC and has adjustable acceleration, velocity and torque controls. The SmartMotor can be controlled manually using the SmartMotor Interface (SMI) or can be programmed using a language developed for use with SmartMotors.

2.3.3.5 Frame Grabber and Data Acquisition System

Images are collected using VisionNow, a frame grabber developed by Boulder Imaging. Use of the software allows real-time image viewing as well as image

acquisition. Images are collected in tagged image file (TIF) format, which is commonly used to collect image data.

2.3.3.6 Analog Output System

TTL trigger signals for both the camera timing and the flashpac timing are sent using Matlab 7.1 and a National Instruments PCMCIA DAQCard-6715. The DAQCard is a high-speed, 12 bit analog output card with 8 channels, each with resolution of 1 MS/s.

2.4 Experimental Considerations

Sediment transport and multiphase flow in the natural environment is a complicated process. It is almost impossible to completely model all of the physical processes involved in the laboratory. Yet the intent of this thesis is not to model sediment transport in the natural environment but rather study a specific, if not primary, cause of erosion. Focusing on one specific condition (the sheet flow condition) eliminates uncertainties that would make the development of a new technique difficult. Since bed forms are constantly being sheared, the assumption of a constant bed elevation and flow steadiness can be made. This allows data collection over the long time periods necessary to capture a velocity profile over the entire sheet.

To create the steady conditions needed, it is important to provide an adequate amount of sediment to the system. It is believed that saturation levels have been reached in the flume due to the storage of sediment in the attached reservoir. Sand is added to the system until sand begins to visually accumulate in the attached reservoir. Also, there is a certain amount of ramp up time necessary when the pump is started.

Because of this, experiments are not conducted until the flume has a significant amount of time to develop a steady condition.

2.4.1 Sand

Commercial sandbox sand is used for the sediment-laden flow experiments. The sand is obtained in 50 pound bags from the local agricultural supply store. Large debris and pebbles are screened from the sand but the sand is not sieved to a specific grain size. A sieve analysis of the sand is included below, showing a median grain diameter (d_{50}) of 0.25 mm. Over the course of the experiments, the flume is been filled and drained several times. This essentially washes the sand and eliminates much of the finer particles.

The sieve analysis is performed at the location of the boroscope, after the flume has been filled and drained several times and several experimental conditions were performed. The kink in the sieve analysis at a particle diameter near 0.2 mm might be explained by a sorting process during any part of the experimental process. Additional sieve analyses should be performed and examined.

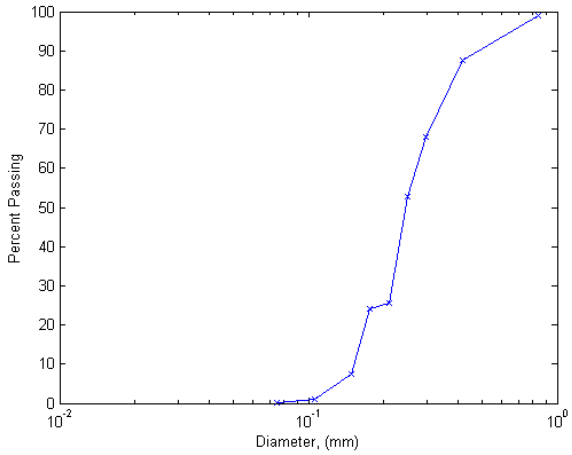

Figure 2.1 Sieve Analysis

2.4.2 Instrumentation Constraints

Excluding the free surface measurements, all of the data collection techniques are intrusive. Both the Nortek Vectrino and the SonTek ADV have a distance to sampling volume of 5 cm, which is far enough to eliminate effects from the transducer head. This distance to sampling volume is both an advantage and a disadvantage, as this limits the amount of water column that can be measured to a depth of at most 5 cm below the free surface. Although the distance to sample volume is fixed at 5 cm, the sample volume size is adjustable for the Vectrino. Reducing the sample volume size is beneficial for high shear regions but a reduction in size brings reduced signal and more data point drop outs. The velocity range is also adjustable. A higher velocity range increases the noise in the system but a velocity range that is too low can produce unreliable data due to decorrelation from shear and/or velocity aliasing. For the sediment-laden flow experiments, a velocity range of ±2.5 m/s is used, which corresponds to a true horizontal velocity range of 3.28 m/s and a true vertical velocity range of 0.94 m/s. A larger velocity range is selected because bulk quantities are of

greatest interest and post-processing algorithms are designed to filter out noisy data. A larger velocity range is also necessary to investigate the sharp gradients found in the boundary layer, which is a major component of this thesis.

The sampling volume for the boroscope is somewhat unclear. The boroscope is simply a lens with an infinite field of view. This is not unlike other imaging systems, in which the camera and lens are outside of the imaged flow. The sampling volume in the more traditional systems is often established by a two-dimensional laser light sheet at the sampling location and the sampling volume is determined by the location of the light sheet as well as the location of the camera and the lens used. This is not the case with the boroscope, where light is delivered through separate fibers in the boroscope itself. Rather than a two-dimensional light sheet, light delivery in the boroscope is fully three-dimensional. Additionally, light is not uniform across the image because of light delivery from a separate window. Diagram 2.3 highlights the difficulties with the separate light delivery and imaging windows. This creates an ambiguity regarding the physical dimensions of the sampling volume as well as the location of particles within the sampling volume. This ambiguity will be addressed in greater detail when discussing aspects of the boroscope development.

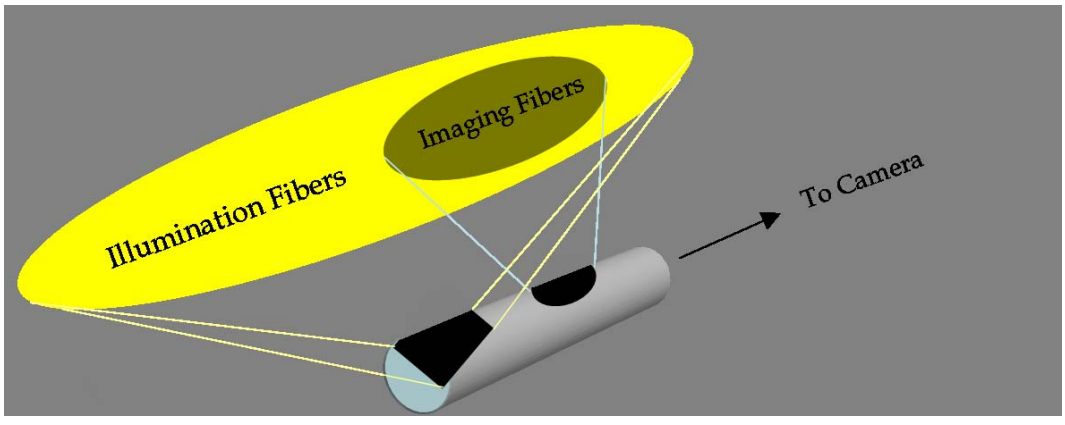

Diagram 2.4 Imaging and Light Delivery Windows

CHAPTER 3

CLEAN WATER FLOW MEASUREMENTS

All clean water flow data is collected using a SonTek 10 MHz Acoustic Doppler Velocimeter (ADV) at a rate of 25 Hz. The ADV has a sampling volume of 0.25 cm^3 with a total sampling volume height of 9 mm. The flow is seeded with microspheres to improve the signal-to-noise ratio. ADV samples are taken on the flume centerline, starting at a location 4 m from the inlet.

Conditions for the clean water flow experiments are shown in Table 1. The flume behavior is evaluated based on the equation for development length over a flat plate:

$$\frac{h}{x} = 0.377\left(\frac{\upsilon}{ux}\right)^{\frac{1}{5}} \qquad (3.1)$$

where h = water depth, x = development length, υ = kinematic viscosity and u = average velocity. Water depths and velocities are chosen to keep the development length between 5 and 7 m according to the equation of development length shown above in Equation 3.1.

Table 3.1 Conditions for clean-water flow experiments

Experiment Date	10/15/04
Depth, h (cm)	12.3
Aspect ratio, b/h	4.8
Slope, S	0.001
Temperature, T (°C)	14.7
Estimated average velocity, u, (cm/s)	22
Calculated development length, x, (m)	5.28
Estimated Froude numbers	0.19

Clean water velocities are resolved in the streamwise (U), cross-stream (V) and vertical (W) directions as shown in the diagram below. Velocity profile data is collected at distances of 4, 5, 6 and 7 meters from the inlet to determine flow development with distance.

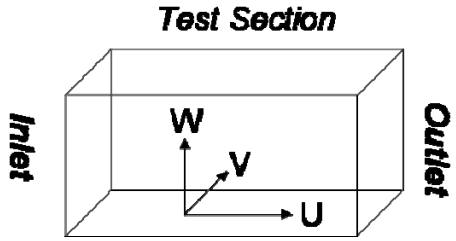

Diagram 3.1 Velocity Directions

Approximately two minutes of data is collected at each point. The raw data is filtered using a signal-to-noise threshold of 18 as well as an adaptive Gaussian filter with a three-sigma threshold. Average velocity profiles are shown in Figure 3.1 for the four test sections.

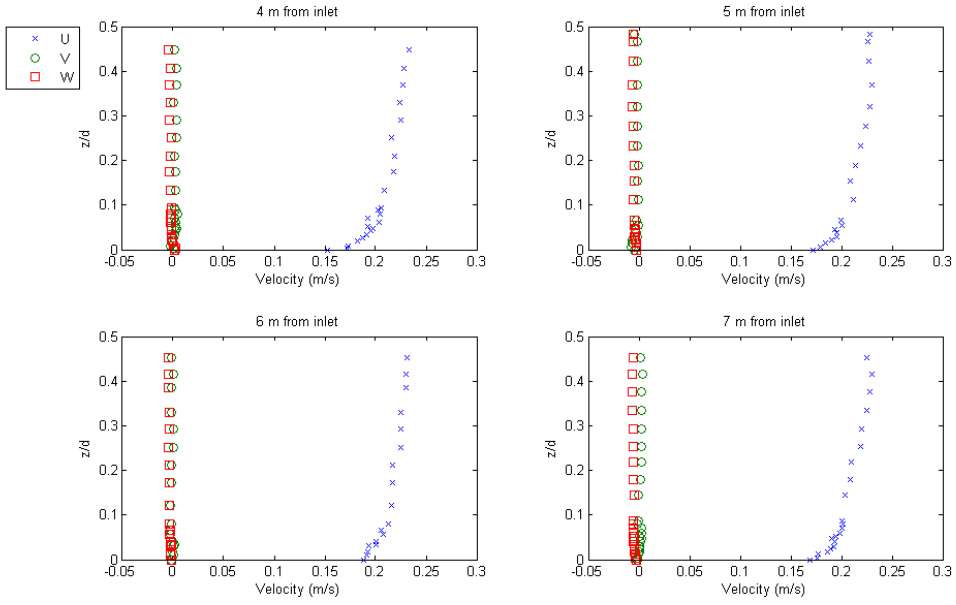

Figure 3.1 Clean Water Velocity Profiles

Cross-stream and vertical velocities remain near zero throughout the water column at all four locations, leading to the assumption of unidirectional flow. Streamwise velocities are shown in Figure 3.2 along with the commonly used Kármán log-law for fully developed flow:

$$u^+ = \frac{1}{\kappa}\left(\ln z^+\right) + C \tag{3.2}$$

where $u^+ = u/u_*$, $z^+ = u_* z/\upsilon$, u_*=frictional velocity, κ=von Kármán's constant, z=vertical location, υ=kinematic viscosity and C is a Reynold's dependent fitting parameter. Frictional velocity was determined by fitting the Kármán log-law using established clean water flow values of 0.41 and 5.5 for κ and C, respectively. Values of frictional velocity, von Kármán's constant and the fitting parameter are given in Table 3.2.

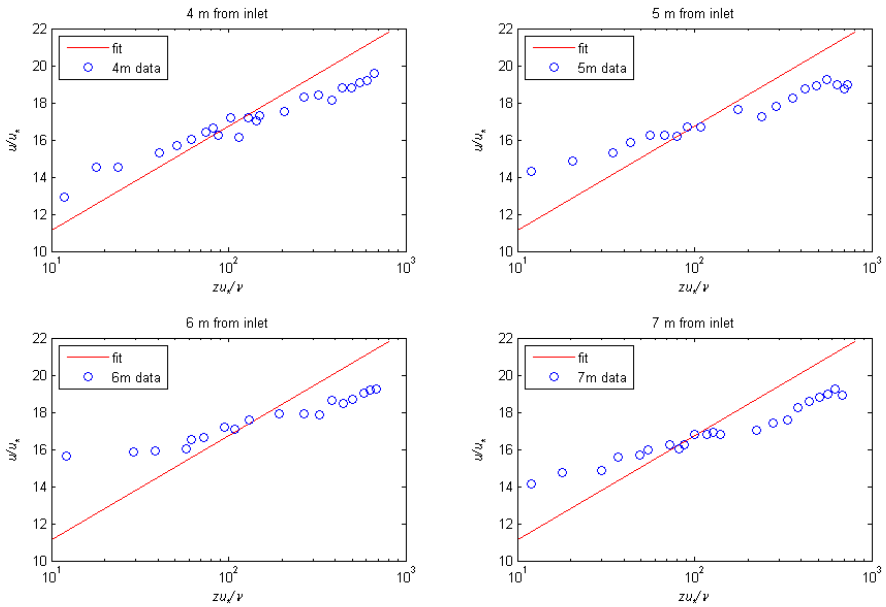

Figure 3.2 Clean Water Streamwise Velocity Profiles

Table 3.2 Logarithmic Fitting Parameters

Value	4 m	5 m	6 m	7 m
u_* (cm/s)	1.19	1.20	1.21	1.20
κ	0.41	0.41	0.41	0.41
C	5.5	5.5	5.5	5.5

For clean water turbulent flows over a flat boundary, κ=0.41 is a widely accepted value. This value is fixed for the log-law fit at each location. The fitting parameter C is also fixed in order to determine a value for frictional velocity, even though C is dependent on a Reynold's number that changes with distance from the inlet. The table also shows consistent values of frictional velocity at each location, indicating the flow has become fully developed by the predicted location.

Clean water experiments verify the validity of the flume for unidirectional flow based on established theory for development length and log-law profiles for turbulent flow over a flat plate. The clean water experiments also highlight the limitations of the open channel flume. Uniform flow conditions are restricted by both the inlet effects (through the development length) and outlet effects (through the drawdown), which are additionally constricted with the addition of sand to the flume. This significantly limits the range of uniform flow conditions within the flume, making uniform flow unachievable under sheet flow conditions.

Finally, there are some concerns over the validity of the clean water flow data. As a check, frictional velocity was calculated based on the shear stress according to the relationship:

$$u_* = \sqrt{gRS} \tag{3.3}$$

where R is the hydraulic radius (0.0872 m) and S is the slope (0.001 m/m). This relationship results in a frictional velocity of 2.93 cm/s, more than twice the values determined by fitting the well established log-law to the measured data. The questionable clean water flow data was discovered after the recirculating flume was filled with sand, making additional clean water flow measurements difficult and time consuming. Since this thesis does not focus on clean water flow measurements, the data was not re-taken and although the individual data is questionable, evaluating the data in reference to each other is considered useful to provide an understanding of the performance and limitations of the recirculating flume. Additional clean water flume studies are encouraged in the future.

CHAPTER 4

SEDIMENT-LADEN FLOW MEASUREMENTS

4.1 Flow Steadiness

Although the clean water experiments verify the validity of the flume, the velocity and depth conditions necessary to create uniform flow are lower than those necessary to create sheet flow when sediment is added to the flume. The length of the flume prevents data collection in a section of uniform steady flow at sheet flow conditions. Although uniform flow is not achievable by its strict definition, here it will be assumed the flow is relatively uniform if the water surface elevation remains steady and parallel to the bed over the measurement section. To verify this, velocity and free surface measurements are taken to determine the steadiness of the flow.

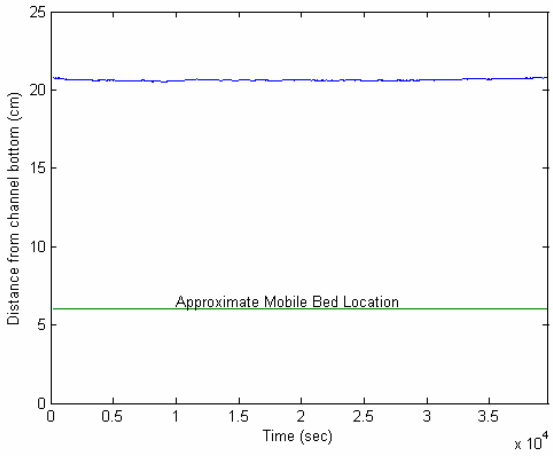

Figure 4.1 Free Surface Measurement

Figure 4.1 shows the location of the free surface over a period of more than 10 hours. A 10-minute moving median is applied to smooth the data. Figure 4.2 below shows the same data as above with the same 10-minute moving median applied. Over

a period of more than 10 hours, the free surface varies by less than 0.5 cm. The free surface was measured using S18U ultrasonic meters which were attached to the frame of the flume. The rigid flume bed was used as a reference datum for depth measurements.

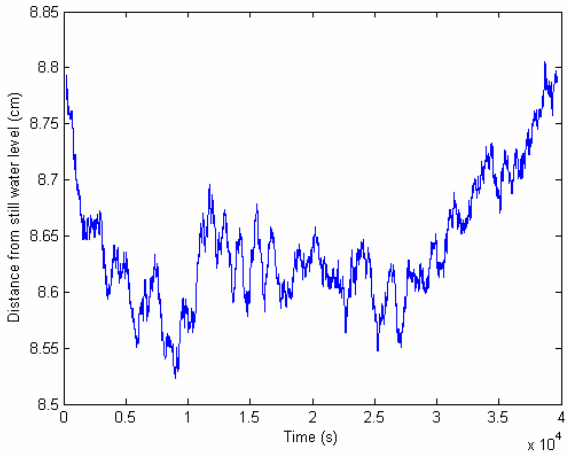

Figure 4.2 Free Surface

A Nortek Vectrino is also used to determine free stream velocities at a constant elevation. Streamwise velocities are plotted in Figure 4.3, with a 10-minute moving median also applied. The figure shows a slight increase and then decrease of velocity over a period of more than 10 hours, although the difference is on the order of only 2 cm/s. The velocity and free surface seem to be somewhat correlated as well. Assuming the sediment bed elevation remains constant, a decrease in free surface elevation should correspond to an increase in streamwise velocity and this appears to be the case with the ADV and wave gage measurements.

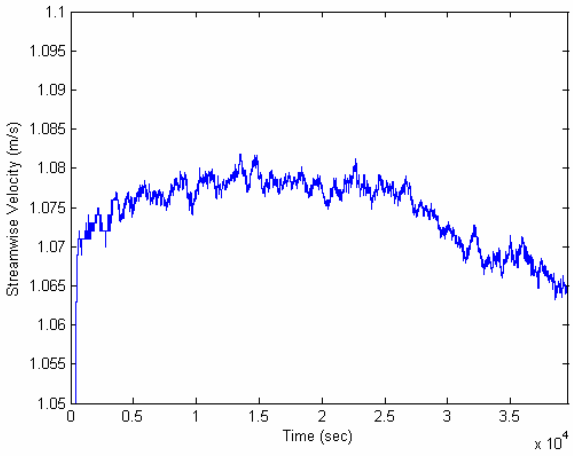

Figure 4.3 Streamwise Velocity

Although the streamwise velocity and free surface changes over time, these changes are insignificant over the 10 hour period. This helps support the assumption of steadiness at the measurement location. There is still concern that the elevation of the sediment bed also changes over time. The determination of sediment bed elevation is complicated by the difficulties of underwater measurement as well as the lack of a clear boundary between the top of the sediment sheet and the suspended portion of the flow. The apparent correlation between velocity and free surface elevation implies that the sediment bed elevation remains constant.

4.2 Velocity Profiles

Velocities are measured for the suspended region above the location of the boroscope to capture a complete velocity profile from the non-moving bed to the free stream. It is important to note that the Vectrino uses an acoustic technique that relies on particles in the flow to reflect the signal and determine velocities. The velocities measured by the Vectrino are particle velocities, not fluid velocities. The Vectrino is not able to differentiate between heavier sediment particles and neutrally buoyant

particles, meaning the suspended velocities are some bulk combination of sediment and fluid velocities. It is assumed that, especially at higher elevations in the water column, the heavier sediment particles have settled and the sediment and fluid velocities are nearly the same.

The vertical profile is achieved by starting data collection at a point below the expected location of the bed and profiling through the sheet layer and into the free stream. Figure 4.4 displays profiles for the streamwise, cross-stream and vertical median velocities which have been filtered using a signal-to-noise ratio threshold of 24.5, an amplitude threshold of 150 counts and an adaptive Gaussian filter with a three sigma range.

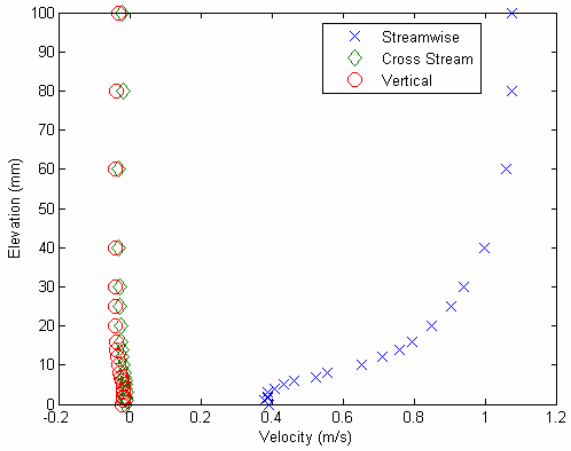

Figure 4.4 Sediment-Laden Velocity Profiles

Comparison of the sediment-laden and clean water velocity profiles is attempted using the Kármán log-law analysis presented in the clean water flow section. The streamwise velocity profiles for both the sediment-laden and clean water experiments are shown in Figure 4.5, normalized by the frictional velocity (log law fitted frictional velocity for the clean water profile, shear stress calculated frictional velocity for the sediment-laden profile) to account for different flow conditions. As

mentioned previously, the clean water data is questionable. Yet simply as a comparison, the clean water and sediment-laden profiles exhibit very different configurations.

The behavior of the sediment-laden streamwise velocity profile clearly differs from the clean water profile suggesting a different and perhaps dynamic von Kármán's constant from the clean water value of 0.41. Logarithmic fitting to determine the value of von Kármán's constant is achieved using u_* =6.42 cm/s (calculated using Equation 3.3 and a slope of 0.004 m/m). As a check, frictional velocity was also estimated by extrapolating the Reynold's stress (shown in Figure 4.6) to the bed, which resulted in a frictional velocity of 4.47 cm/s. It is unclear why the Reynold's stress approximation is lower than the frictional velocity calculated from the shear stress or if the use of the Reynold's stress as an approximation is even valid for sediment-laden flows. It is presented here merely as a check, additional analysis presented in this thesis will use the frictional velocity calculated from shear stress, 6.42 cm/s.

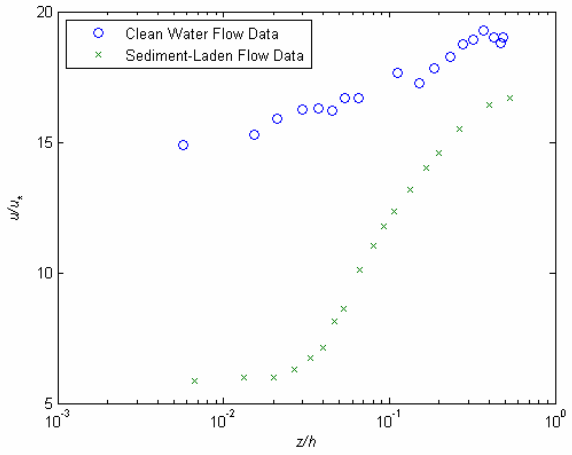

Figure 4.5 Sediment-Laden and Clean Water Streamwise Velocity Profiles

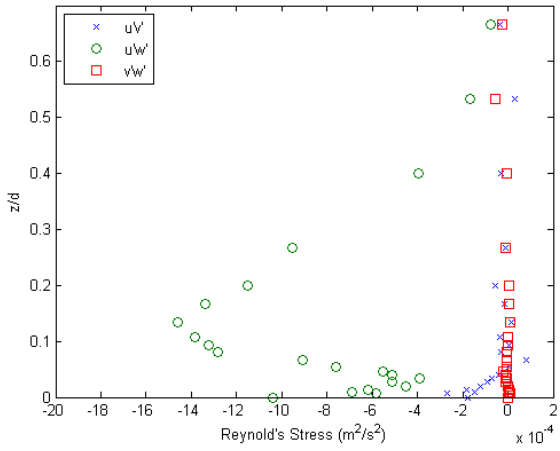

Figure 4.6 Sediment-Laden Reynold's Stress Profiles

Figure 4.7 displays the sediment-laden streamwise velocity profile with two logarithmic fits. The frictional velocity is kept constant while the value of von Kármán's constant is reduced to 0.16 and 0.29. Vanoni (1957) observed an increase in velocity gradient and thus a decrease in the value of κ, which he explained as a damping of turbulence caused by the suspended material. Ippen et al. (1966) also reported a non-constant value of κ for sediment-laden flow with values ranging from 0.168 to 0.218, suggesting that a different law altogether should apply to the bottom of the channel where the concentrations are greater.

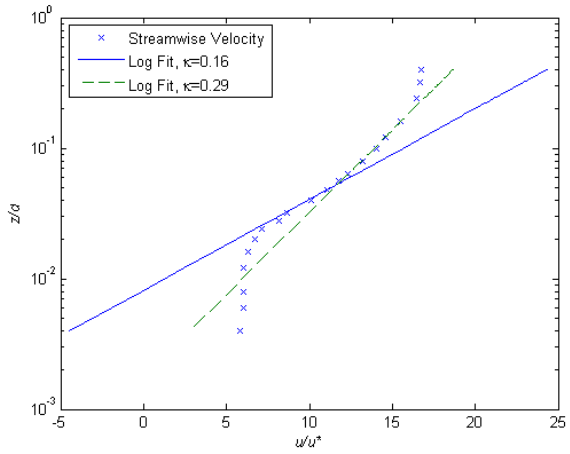

Figure 4.7 Streamwise Velocity Logarithmic Fit Curves

Recent work by Bennett et al. (1998) questions the use of differing κ values and instead suggests the clean water value of 0.41 should be retained and a new parameter, a flux Richardson number, should be introduced that accounts for density stratification. Without information on the sediment concentration in the water column, which was not collected as part of this study, the application of a flux Richardson number is infeasible. Future experimental work should make attempts to measure sediment concentration concurrently with velocity throughout the entire water column.

4.3 Sheet Elevation

To capture the full range of velocities above the sheet, ADV measurements are examined in real-time to determine the vertical position that corresponds with the smallest streamwise velocity. The ADV is then placed below this point and moved stepwise up to collect a profile of the entire water column. This enables the capture of velocities within the entire water column but raises an uncertainty over the location of the non-moving bed. This results in the need to shift the location of velocity profiles and possibly remove data invalidated by the presence of the bed.

Determining the location of the top of the sheet layer and thus the start of the suspended velocity profile is challenging yet critical. Along with velocity, the Vectrino records correlation (how well the velocity agrees with itself, measured in a percentage), amplitude (the strength of the signal in counts) and signal to noise ratio. These metrics are shown below in Figure 4.8 along with the streamwise velocity. The signal to noise ratio is high, as expected for a heavily-seeded flow, but behaves strangely near the bed. The streamwise velocity is also strange near the bed, with a small decrease in velocity in the first few measurements. A closer examination of both the streamwise velocity and the signal to noise ratio for the first 10 mm of measurement is shown in Figure 4.9.

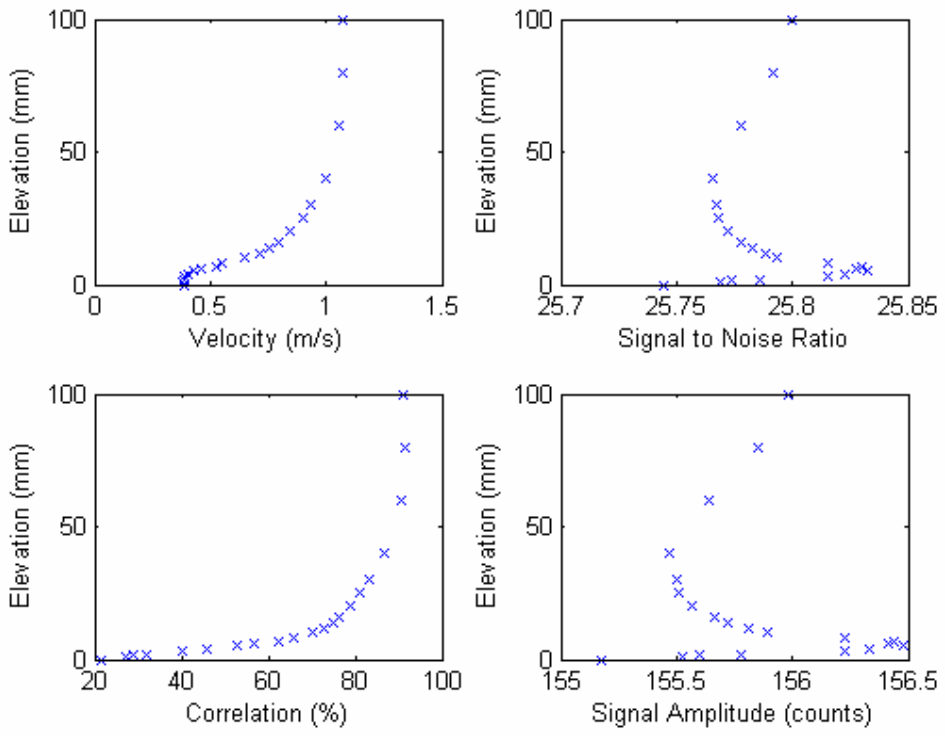

Figure 4.8 ADV Metrics

The ADV measurements begin at a location below the bed elevation, which allows for the ADV to profile from the fixed bed through the sheet layer and into the free stream. The acoustic technique prevents the measurement volume from penetrating the fixed bed, which is complicated by the signal dispersing effects of the highly-concentrated sheet layer. Most likely, the high sediment concentration prohibits the ADV from recording accurate measurements through the entire sheet layer into the fixed bed yet it is reasonable to assume the ADV measurements partially penetrate the sheet layer.

From Figure 4.9, the velocity begins to increase between 3 and 4 mm from the initial measurement location and continues to increase as the ADV profiles upward in accordance to the logarithmic profile shown in Figure 4.7. The 3 mm location appears to be the beginning of valid velocity vectors. This velocity measurement appears to be located within the thin sheet layer, as the signal-to-noise ratio continues to increase to a maximum value near the 5 mm location.

Variations in the signal-to-noise ratio are perhaps not a true indication of the location of the sheet, especially considering how negligible the signal-to-noise ratio variations are over the entire water column. Yet, as stated previously, it is not unreasonable that the ADV has the capability to penetrate a portion of the sheet layer to measure valid velocities. Figure 4.9 shows a decrease in velocities below the elevation of the maximum signal-to-noise ratio. For the purposes of this thesis, these measured velocities will be considered valid. It is also interesting to note that, although the measured velocities remain relatively constant in the first 3 mm of elevation, the signal-to-noise ratio increases with elevation until it reaches the maximum near the 5 mm location. While a powerful experimental tool, more understanding of the ADV's capabilities is needed to establish confidence in measurements taken at the limits of the equipment. As the top of the sheet layer

represents the outer most extents of both the ADV and the newly developed boroscope, research on this area will be necessary to produce a complete sediment-laden velocity profile. That investigation is beyond the scope of this thesis and, as an initial trial, signal-to-noise ratio will be used here to determine the location of the sheet.

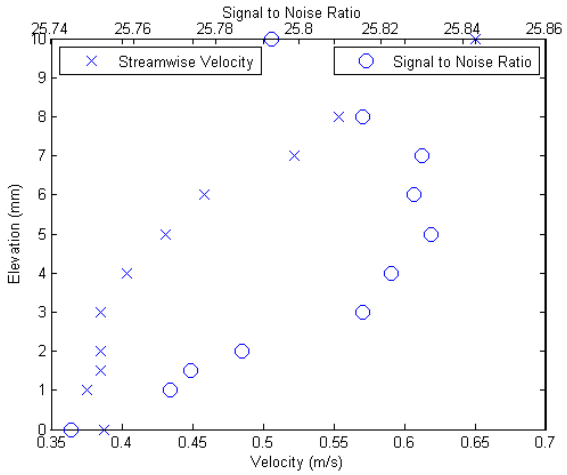

Figure 4.9 Streamwise Velocity and Signal to Noise Ratio, First 10 mm

Although velocity measurements are determined to be valid starting at the 3 mm location, this does not place the data at any physical elevation in reference to the bed. The physical location of the suspended velocity profile in reference to the bed must be verified by a separate measurement technique, namely the boroscope. Boroscope development and calibration is described in the following chapter.

CHAPTER 5

BOROSCOPE DEVELOPMENT

5.1 Boroscope Generations

A variety of boroscopes were designed and tested in the process of developing the final technique. In initial designs, the imaging window was located at the end of the boroscope, so that the scope acted much like a conduit between the camera and the image of interest. The imaging boroscope was surrounded by a ring of light delivery fibers. This created a cone of light that increased with distance from the scope tip. This also created a small region that didn't receive any light, from very near the scope tip until a distance away from the scope tip where the ring of light was able to disperse and cover the entire image area. This dark region was unacceptable, considering sediment blocking effects restricts the field of view to very near the scope tip in dense flows. Additionally, the location of the viewing window restricted data collection to the x-y plane, eliminating the ability to capture vertical fluxes.

A 90° mirror sleeve was created to address these problems. The sleeve could be slid over the boroscope and contained an angled mirror at the end that adjusted the field of view by 90° so that the imaging window could either be placed in the x-z plane or the y-z plane. The distance between the scope tip and the mirror as well as the mirror and the sleeve wall allowed the light to diffuse, eliminating dark regions within the flow. While the mirror sleeve solved some problems, it created others. The opening between the mirror and the sleeve wall (necessary for imaging) allowed particles from the flow to enter. Particles near the mirror could be imaged twice in the same image (the image would "see" both the original particle and the mirrored

particle). This made it impossible to determine the location of the particle or differentiate between real particles or their mirrored partners.

To address these problems, a scope was developed with a 90° sealed prism at the end of the imaging fiber. The result was a completely sealed scope with an imaging window that was flush to the scope wall that allowed imaging in the x-z and y-z planes. Use of the sealed prism solved the problem of mirrored particles but it necessitated a change in the location of the light delivery fibers. The optical properties of the prism prevented both imaging fibers and light delivery fibers to run through it so a separate window was created for light delivery that was closer to the scope tip. This window was beveled to increase the output light angle from the scope to about 120°. The light delivery and imaging windows are separated by a distance of 1.5 mm. This distance also creates a dark region close to the imaging window as well as a gradient of light intensity across the image.

5.2 Image Capture

Both the camera and the flashpacs are driven with TTL pulses, which are sent by the DAQCard. The camera triggers on the falling edge of a TTL signal while the flashpacs trigger on the rising edge of a TTL signal. DAQCard constraints require the use of two channels for driving the camera and two flashpacs. To achieve separate flashpac timing, an opto-isolator and a switch are placed on one of the DAQCard channels. This allows the use of both positive and negative triggers to differentiate between flashpacs. The image acquisition triggering is shown in Diagram 5.1.

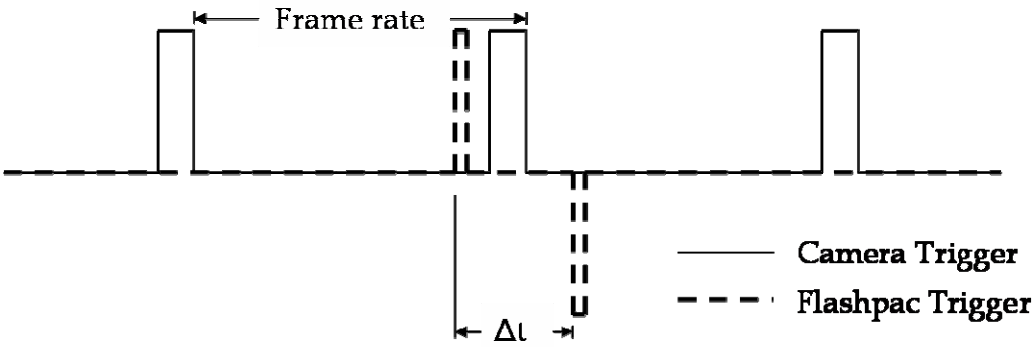

Diagram 5.1 Camera and Flashpac Timing

5.3 Particle Image Velocimetry

Sediment velocities are calculated using Particle Image Velocimetry (PIV) techniques. PIV techniques are plentiful and have been extensively researched and published. For more detailed information about PIV techniques and their applications, the reader is encouraged to read PIV and Water Waves (Grue et al. 2004).

5.3.1 Minimum Quadratic Difference

Imaged particles can be tens of pixels in size and can be either light or dark, which is much different than traditional imaging techniques that utilize small particles that are illuminated against a black background. Non-uniformities in particle distribution and illumination make it ideal to use Minimum Quadratic Difference (MQD) instead of traditional correlation or tracking algorithms to calculate sediment velocities (Gui and Merzkirch 2000). MQD is better suited to analyze patterns in the flow rather than particles (Helmle 2005).

The MQD routine utilizes an initial subwindow (S1) from the first image in the pair and a second subwindow (S2) from the same location in the second image of the pair that is larger by a user-defined radius. To determine pixel displacement, S1 is moved through every possible location within S2. The pixel values from S1 are subtracted from the pixel values in S2 and squared. The squared differences at each subwindow location are summed to create the MQD matrix. The pixel displacement is located at the minimum value of the MQD matrix. Subpixel fitting is accomplished using a first-moment centroid method. A 5x5 matrix, centered on the minimum value of the larger MQD matrix, is used for the analysis. The subpixel fitting method limits displacement analysis to pixels within the range $3 < x <$ (Subwindow Radius-2) and $3 < y <$ (Subwindow Radius-2).

5.3.2 Image Pre-Processing

Images are processed before running through the MQD routines to improve image quality.

5.3.2.1 Low Pass Filter

A two-dimensional low pass filter is used to remove noise from the image. A pixel-wise adaptive Wiener method is used, with statistics for the filtering based on a 3x3 neighborhood around each pixel.

5.3.2.2 Median Filter

After the low pass filter, the images undergo two-dimensional median filtering. Pixels are set to a median of the pixels in a 3x3 neighborhood. Median filtering is well suited to remove outliers without reducing the sharpness of the image.

5.3.2.3 Histogram Equalization

The final pre-processing step involves histogram equalization. Histogram equalization transforms intensity values so that the histogram of the output image matches a uniform distribution. This effectively enhances the contrast of the image.

Image 5.1 shows the effect of the previous pre-processing techniques on a given image.

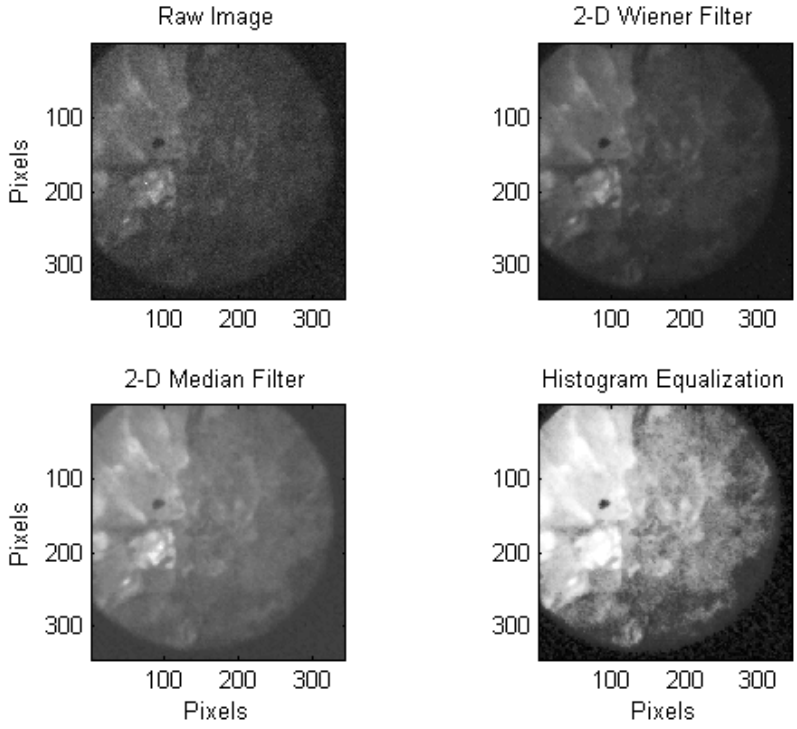

Image 5.1 Image Filtering

5.3.2.4 Minimum Image Removal

In addition to the pre-processing techniques discussed, Cowen and Monismith (1997) suggest removal of the minimum image from the data set before processing the images. Helme (2005) found that removal of the minimum image was not beneficial when using the MQD technique, as MQD evaluates high and low intensities the same. When testing the MQD routine, the mean image was calculated and removed but this made data sets with small pixel displacements unreliable. Since the signal in the images is low to begin with, the removal of the mean seems detrimental to the calculation of pixel displacements.

5.3.3 Subwindow Determination

Subwindow sizing is important for several reasons. The full boroscope image size is 344 pixels x 344 pixels. The use of smaller subwindows for displacement calculations allows for multiple velocity determinations across the 2-D image, making gradient determination in an image possible. The use of a smaller subwindow is also critical to computation time. The amount of computation time required for displacement calculation scales directly to subwindow area, the larger the subwindow the longer the computation. With the extensive amount of data collected, computation time is non-trivial. Tests are run on subwindow sizes of approximately full image, half image and quarter image.

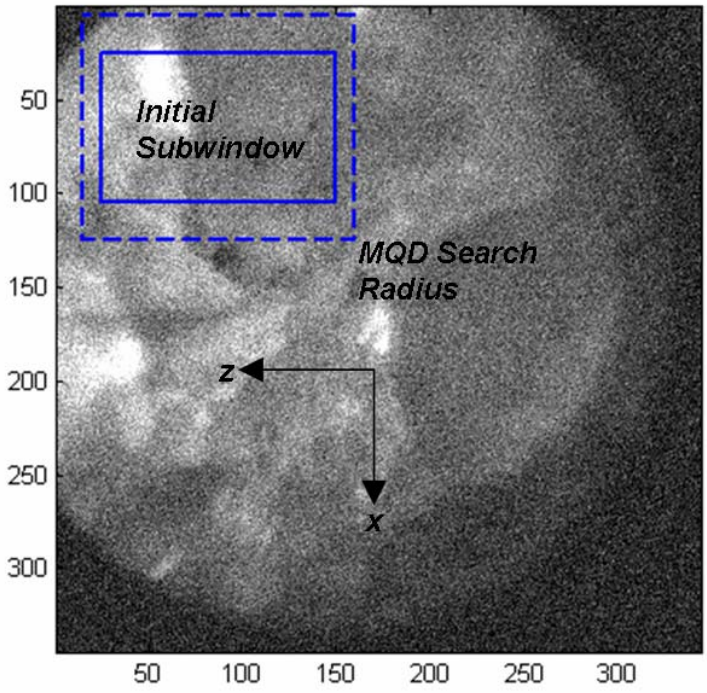

Image 5.2 Subwindow and MQD Search Radius

The subwindow selected for use (shown in Image 5.2) in displacement analysis consists of a 125 by 80 pixel window with a search radius of 10 pixels in the vertical direction and 20 pixels in the horizontal direction. This subwindow size limits the amount of computation time while taking advantage of the gradient of light across the image. It also allows for the possibility of adding additional subwindows in future image analysis efforts.

5.4 Calibration

More important than the ability to capture images of sediment grain displacements is the process of converting the displacements into physical distances. Due to the infinite field of view of the lens, the corresponding physical dimension of

the imaging window increases with distance from the scope wall. The absence of a two-dimensional light sheet presents the problem of determining particle location. This is compounded by the fact that a significant range of particle sizes as well as particle shapes are present in the flume. At different vertical locations within the sheet flow layer, changes in sediment concentration and possibly even sediment sorting require a dynamic calibration. Three different methods were developed in an effort to create this dynamic calibration.

5.4.1 Fixed Calibration

An initial calibration technique examines the size of an object at different distances from the scope tip. To determine how the physical dimension of the image changes with distance from the scope tip, a wire of known diameter is attached to a brown background. The wire and background is attached to a positioning system in order to step the wire away from the scope tip at known distances. An image of the wire is taken at every distance from the scope tip. Since the physical width of the wire is known, the width of the wire in pixels in a representative image is used to develop a ratio of pixels to millimeters. This ratio is converted to a physical window size using the width of the image, in this case 344 pixels, at each known distance from the imaging window. The resulting relationship between physical image size and distance from the scope tip is shown in Figure 5.1.

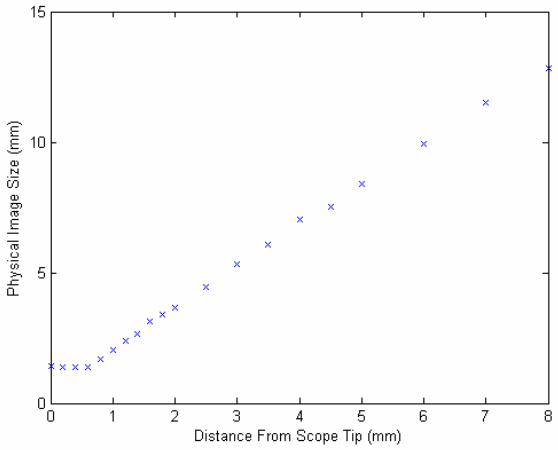

Figure 5.1 Fixed Calibration

As expected, the figure shows a linear relationship between image size and distance from the scope tip. This type of calibration is typically used in traditional PIV measurements where the field of view is two-dimensional and located at a fixed distance from the camera.

5.4.2 Moving Calibration

A more robust approach utilizes a moving calibration, where physical image size with distance from the scope tip is determined using the MQD technique. Two vertical positioning systems are used for this technique. Several layers of natural sediment taken from the flume are glued onto a rigid background and then attached to one of the positioning systems, which allows the sediment plate to step away from the scope tip at known distances (determining how the physical dimension of the imaging window changes with depth into the flow). The boroscope is attached to the second positioning system and driven along the sediment plate at a velocity of 0.1 mm/s. For safety of the scope it is undesirable to drive at much higher velocities. Image 5.3

shows the moving calibration system set-up along with the movement directions of the positioning systems.

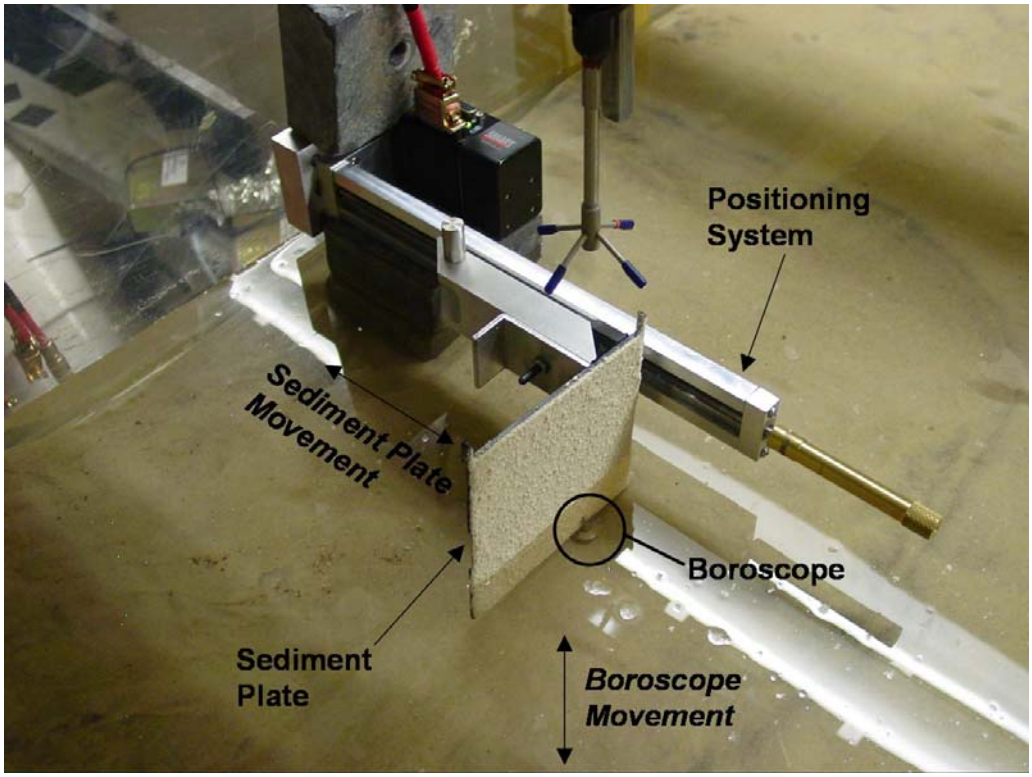

Image 5.3 Moving Calibration System

Image pairs are taken at 10 Hz but the data is downsampled for displacement calculation, creating a Δt between images of 0.5 seconds. The MQD technique is applied to the image pairs, which results in pixel displacements at each location. The raw displacements are filtered to remove bad data points using an adaptive Gaussian filter with a 3 sigma threshold from the mean displacement. Since the Δt between images is known, the ratio of mm/pixel is determined by setting the driven velocity (0.1 mm/s) equal to the pixels per time value at each location (MQD determined displacement/0.5 seconds). The simplified expressions to determine physical image size are shown below:

$$\frac{mm}{pixel} = \frac{MQDdisplacement}{(0.1)*(0.5)} \tag{5.1}$$

$$\Theta = \frac{mm}{pixel} * 344\, pixels \tag{5.2}$$

where Θ = physical image size, in mm.

Image sets are collected moving the scope up and down. The mean filtered image sizes are shown in Figure 5.2. A linear trend appears in both the moving up image sets as well as the moving down image sets. This linear trend becomes invalid at distances greater than 5 mm, or approximately 20 grain diameters, from the scope tip. In the highly concentrated sheet flow layer it is unlikely that the scope would image particles greater than 20 grain diameters from the scope tip.

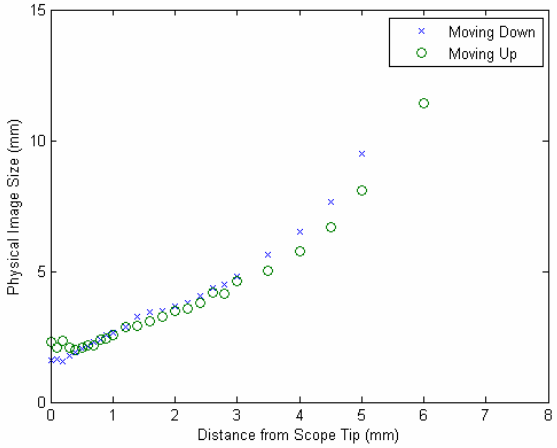

Figure 5.2 Moving Calibration

For comparison, the moving calibration (down image sets) is compared to the fixed calibration in Figure 5.3. There is good agreement between the two methods for determining physical image size. This not only establishes the growth of the image

size with distance from the scope tip but also verifies the MQD routine for pixel displacement.

Applying a linear fit allows the determination of physical image size as a function of distance from scope tip, as shown in the following equation:

$$\Theta = 1.562\delta + 0.5454 \qquad (5.3)$$

where Θ = physical window size and δ = distance from scope tip.

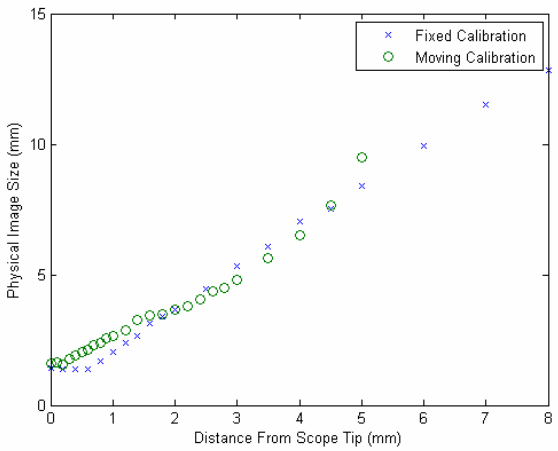

Figure 5.3 Fixed and Moving Calibrations

5.4.3 In-Situ Calibration

The final method for determining physical image size is similar to the moving calibration. Again, the scope is moved at a known velocity to determine the physical window size. While in the moving calibration the sediment particles are fixed in place on a rigid backing, the in-situ calibration occurs in the uncompressed sediment bed. The bed is fluidized under sheet flow conditions, the recirculating pump is stopped and the bed is allowed to settle. The scope is moved up and down through the bed at

rates of 0.1, 0.2 and 0.3 mm/s. Images are collected at a rate of 10 Hz, giving a Δt of 0.1 seconds. Details of the trial runs are listed in Table 5.1.

Table 5.1 In-Situ Calibration Trials

Trial 1	0.1 mm/s, Δt = 0.1 s, moving up for 1 minute
Trial 2	0.1 mm/s, Δt = 0.1 s, moving up for 1 minute
Trial 3	0.1 mm/s, Δt = 0.1 s, moving down for 1 minute
Trial 4	0.1 mm/s, Δt = 0.1 s, moving up for 1 minute
Trial 5	0.1 mm/s, Δt = 0.1 s, moving down for 1 minute
Trial 6	0.2 mm/s, Δt = 0.1 s, moving up for 1 minute
Trial 7	0.2 mm/s, Δt = 0.1 s, moving down for 1 minute
Trial 8	0.2 mm/s, Δt = 0.1 s, moving up for 1 minute
Trial 9	0.2 mm/s, Δt = 0.1 s, moving down for 1 minute
Trial 10	0.3 mm/s, Δt = 0.1 s, moving up for 1 minute
Trial 11	0.3 mm/s, Δt = 0.1 s, moving down for 1 minute
Trial 12	0.3 mm/s, Δt = 0.1 s, moving up for 1 minute
Trial 13	0.3 mm/s, Δt = 0.1 s, moving down for 1 minute

The raw displacements are filtered using an adaptive Gaussian filter with a 3 sigma threshold from the mean displacement. As the velocity of the scope increases, the physical window size asymptotes to a value near 2 mm, as shown in Figure 5.4.

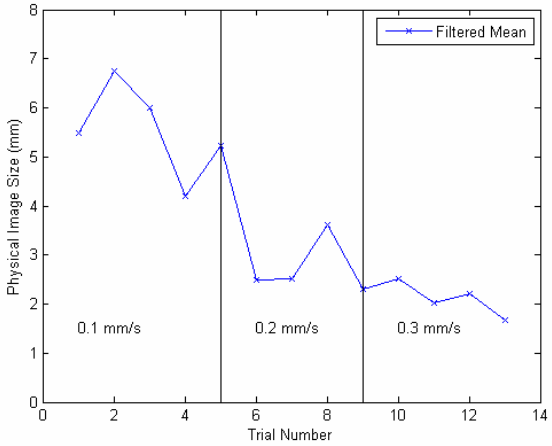

Figure 5.4 In-Situ Calibration

The MQD routine seems to have trouble at low velocities, where pixel displacements are small. To check this, the first five trials are re-processed with a Δt of 0.3 seconds. This is done by downsampling the images and is equivalent to a Δt of 0.1 seconds and a scope velocity of 0.3 mm/s. This re-processed data is plotted, along with the data in Figure 5.4, in Figure 5.5.

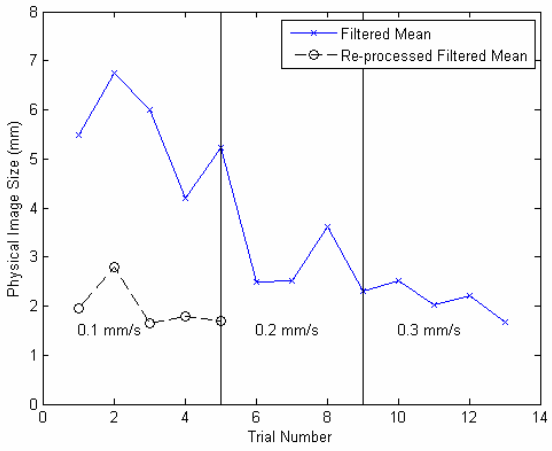

Figure 5.5 In-Situ Calibration, First Set Reprocessed

The physical image size for the re-processed data is similar to that of the 0.3 mm/s trials. For comparison, the mean value of the 0.3 mm/s trials is 2.10 mm while the mean of the re-processed 0.1 mm/s trials is 1.97 mm.

It is possible to use the mean value of 2.10 mm as a constant calibration for the boroscope. While this is an in-situ calibration using real sediment, there are also problems associated with applying this calibration to the entire sheet flow layer. First, a primary assumption with this technique is that the scope does not significantly affect the flow of the fluid/sediment mixture. During the in-situ calibration, the motion of the scope pushes and pulls sediment grains as it is driven through the sediment bed. This dragging and sudden release of particles along the imaging window can

significantly skew the MQD displacement results. Secondly, previous calibrations show that the physical image size changes with distance from the scope tip. As the scope moves up through the sheet flow layer, the sediment concentration decreases and the scope can see farther into the flow. This effectively creates the need for a calibration that is dependent upon the sediment concentration. Since the boroscope moves through the non-moving bed in the in-situ calibration, sediment concentration and distance from the scope remain constant. This prevents the use of the in-situ calibration for a range of sediment concentrations.

5.4.4 Sediment Concentration Metrics

With the need for a dynamic calibration, it is important to look for possible metrics within the images which could relate elevation to physical window size.

Since light exits from a separate window on the scope, light intensity should decrease with distance from the scope. For example, particles close to the scope should show up brighter than particles far from the scope. As it turns out, this is only partially true. Due to the configuration of the scope and the separation between light delivery and imaging windows, full illumination within the subwindow occurs approximately 2 mm away from the scope tip. Because of this, light intensity initially increases until it reaches this point of full illumination, at which point intensity decays with distance as expected.

Light intensity and the variance of light intensity are calculated over the analysis subwindow for both the moving calibration data and the sheet flow layer data. Three methods are developed to determine the distance to the field of view and create a dynamic calibration.

5.4.4.1 Intensity Matching Method

The first technique requires the assumption that intensity values in the initial linear region of the moving calibration should be directly related to the intensity values in the initial linear region of the sheet flow layer data (intensities for both the moving calibration and the sheet flow data can be found in Figures 5.7 and 5.8). Until the peak of full illumination is reached (at an elevation above the bed of ~2 mm), sheet flow layer maximum intensities are fit to the linear region of the moving calibration maximum intensity curve and the corresponding distance to scope tip is determined. Physical image size is obtained using the fixed calibration. Once the peak of full illumination is reached the size of the image window is assumed to remain constant, as is seen in Figure 5.6.

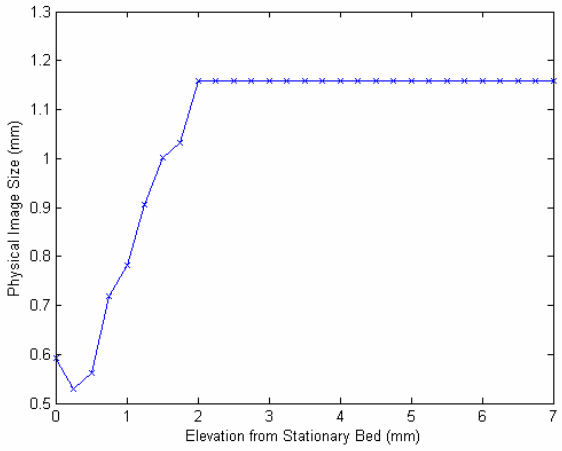

Figure 5.6 Intensity Matching Method

5.4.4.2 Maximum Intensity Method

Each image, for both the moving calibration and the sheet flow layer data sets, contains 344 x 344 or 118,336 total pixels, each containing a value for the intensity. Figures 5.7 and 5.8 show intensity values that represent: the median value, the 25th and 75th percentile value and the 10th lowest (termed minimum) and 10th highest (termed maximum). These intensity parameters are calculated for each image, the figures below show the median value of each of these 5 parameters across the image set.

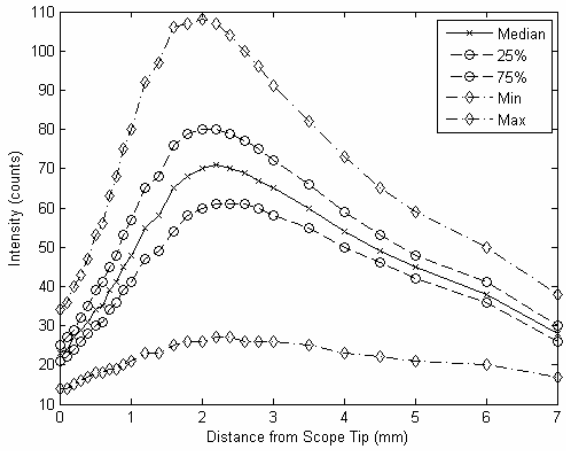

Figure 5.7 Intensities, Moving Calibration

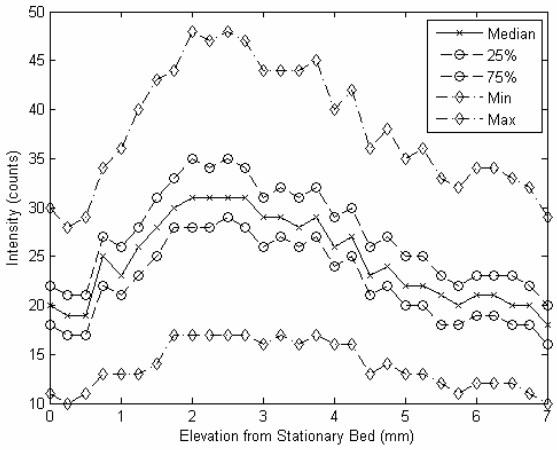

Figure 5.8 Intensities, Sheet Flow Layer

The figures show how the scope configuration causes the intensity to grow linearly until full illumination is achieved. After full illumination is achieved, intensity decreases exponentially with distance. Also, although the figures represent two different experiments, the shape of the intensity curves remains the same.

Intensity, especially the maximum intensity in each image, behaves in a similar manner in both the moving calibration and the sheet flow layer. A linear region exists in highly concentrated regions, suggesting a high concentration of particles near the imaging window is limiting the cone of light from entering the sample volume. The sheet flow layer data also suggests a peak where the cone of light reaches the entire image and then decays as light diffuses with distance. The decay is not as steep as the initial linear increase, which suggests that particles closer to the imaging window (possible in the real data, not in the moving calibration) are decreasing the slope.

The curves are clearly more pronounced for the maximum intensities, with a noticeable peak separating the initially increasing linear region and the exponentially decaying region. This leads to the use of maximum intensities to compare sheet flow layer data with calibration data, creating a dynamic calibration technique.

The intensities are split at the peak intensity value into a linear region and an exponential region. The diffusion of light as the cone fully enters the imaging window creates a smooth transition between the linear and exponential region. Because of this smoothing, the peak intensity value as well as the intensity values on either side of the peak are eliminated from the curve fitting procedure. The maximum intensity values with the fit curves for the moving calibration and the sheet flow layer are shown below in Figure 5.9 and 5.10, respectively.

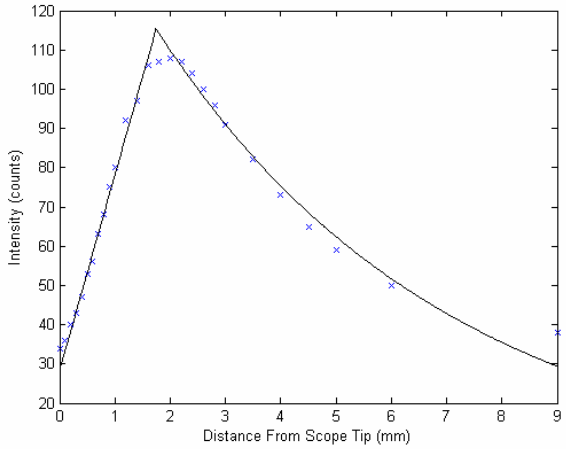

Figure 5.9 Maximum Intensity, Moving Calibration

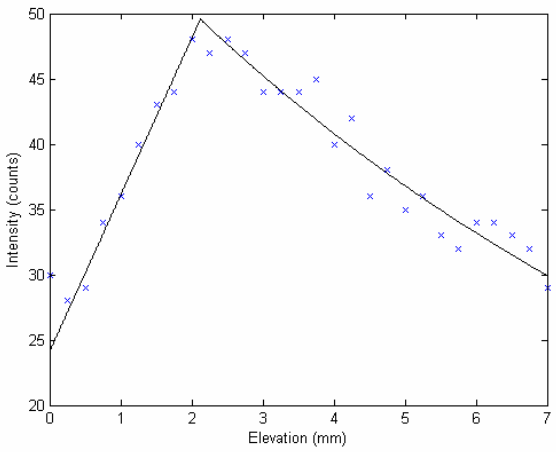

Figure 5.10 Maximum Intensity, Sheet flow Layer

Table 5.2 lists the linear and exponential fits, goodness of fits and the value and location of the peak created by the merging of the two fits. The fit peak is used to normalize the sheet flow data.

Table 5.2 Maximum Intensity Fit Parameters

Moving Calibration	Sheet flow Layer
Linear Fit: y = 49.81x+28.48 R^2 = 0.9931 Exponential Fit: y = 160.1 exp(-0.1882x) R^2 = 0.9740 Fit Peak: 115.3 counts at 1.74 mm	Linear Fit: y = 12x+24.14 R^2 = 0.9811 Exponential Fit: y = 61.69 exp(-0.1032x) R^2 = 0.8916 Fit Peak: 49.6 counts at 2.12 mm

Using the fit peaks for normalization, the sheet flow layer maximum intensities are multiplied by 115.3/49.6, or 2.32. This is a constant factor that is applied to each sheet flow layer data point. Sheet flow layer elevations are converted to distances from the scope tip by using the normalized maximum intensities and rearranging the moving calibration fit curves like such:

For sheet flow elevations < 2.12 mm:

$$\delta = \frac{I - 28.48}{49.81} \tag{5.4}$$

For sheet flow elevations > 2.12 mm:

$$\delta = \frac{\ln\left(\frac{I}{160.1}\right)}{-0.1882} \tag{5.5}$$

where I = intensity in counts.

The distances are converted into physical image sizes at each location using the linear relationship found in the fixed calibration. Figure 5.11 shows the physical image size at each elevation in the sheet flow layer, based on the maximum intensity method.

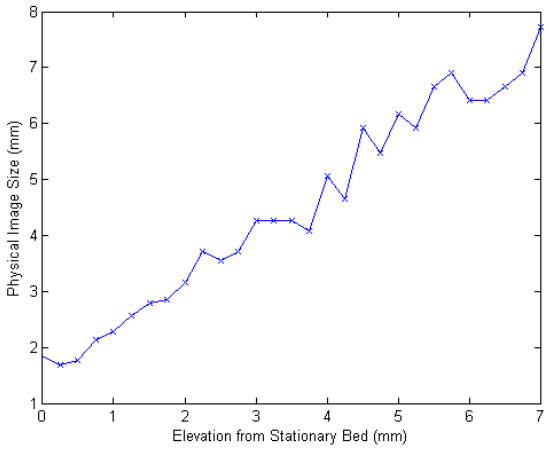

Figure 5.11 Physical Image Size, Maximum Intensity

5.4.4.3 Variance of Intensity Method

Along with the intensity, the variance of the intensity is also examined as a calibration technique. The variance of intensity, which can be thought of as the ratio between light space and dark space, is taken within the subwindow and not over the entire image. A similar approach is taken to the variance of intensity method as the maximum intensity method. The variance of the intensity across the subwindow is calculated for each image. Figures 5.12 and 5.13 show the median variance for both the moving calibration and the sheet flow layer data.

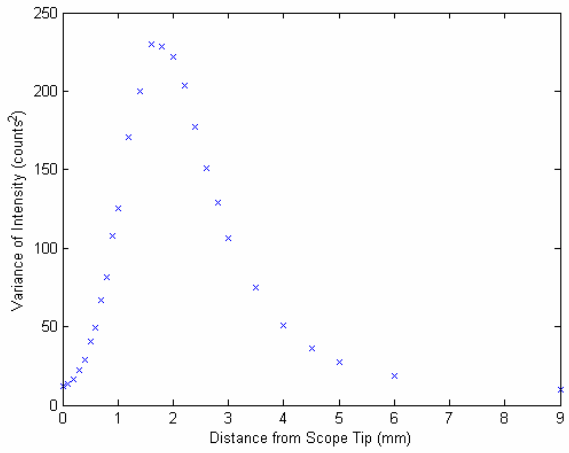

Figure 5.12 Variance of Intensity, Moving Calibration

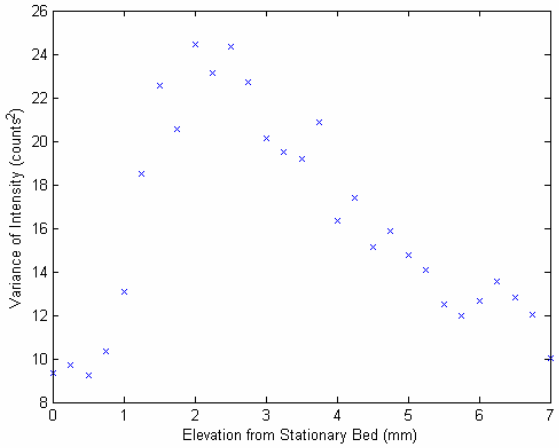

Figure 5.13 Variance of Intensity, Sheet Flow Layer

The variance of intensity is not necessarily expected to vary linearly and exponentially like the maximum intensity. By trial of various curve fits, a quadratic fit was determined best for the initial region and an exponential fit was again applied to the second region.

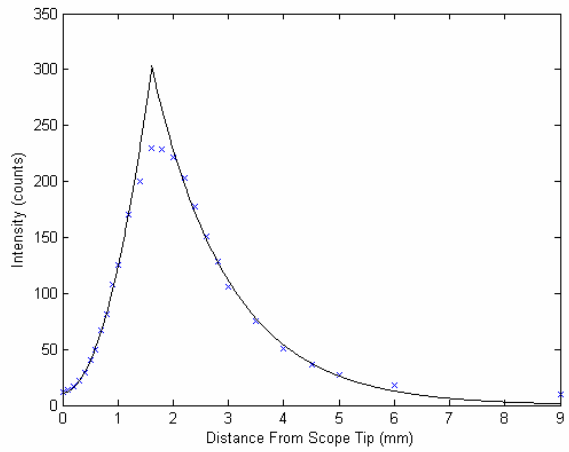

Figure 5.14 Variance Curve Fits, Moving Calibration

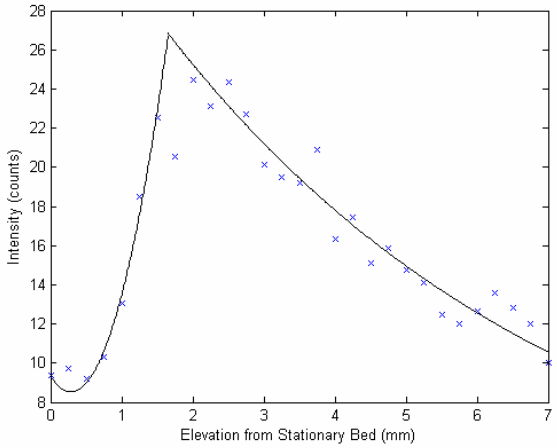

Figure 5.15 Variance Curve Fits, Sheet Flow Layer

Table 5.3 lists the linear and exponential fits, goodness of fits and the value and location of the peak created by the merging of the two fits. As with the maximum intensity method, the fit peak is used to normalize the sheet flow data.

Table 5.3 Variance of Intensity Fit Parameters

Moving Calibration	Sheet flow Layer
Quadratic Fit: $y = 109.7x^2+3.55x+10.74$ $R^2 = 0.9978$ Exponential Fit: $y = 969.6 \exp(-0.7218x)$ $R^2 = 0.9958$ Fit Peak: 302.5 counts^2 at 1.61 mm	Quadratic Fit: $y = 9.748x^2-5.558x+9.33$ $R^2 = 0.9898$ Exponential Fit: $y = 35.79 \exp(-0.1743x)$ $R^2 = 0.9287$ Fit Peak: 26.8 counts^2 at 1.65 mm

Using the fit peaks for normalization, the sheet flow layer maximum intensities are multiplied by 302.5/26.8, or 11.29. This is a constant factor that is applied to each sheet flow layer data point. Sheet flow layer elevations are converted to distances from the scope tip by using the normalized maximum intensities and rearranging the moving calibration fit curves like such:

For sheet flow elevations < 1.65 mm:

$$\delta = \frac{-3.55 + \sqrt{(3.55)^2 - 4(109.7)(10.74 - \varphi)}}{2(109.7)} \tag{5.6}$$

For sheet flow elevations > 1.65 mm:

$$\delta = \frac{\ln\left(\frac{\varphi}{969.6}\right)}{-0.7218} \tag{5.7}$$

where φ = variance of intensity in counts.

The distances are converted into physical image sizes at each location using the linear relationship found in the fixed calibration (Equation 5.3). Figure 5.16 shows the physical image size at each elevation in the sheet flow layer, based on the variance of intensity method.

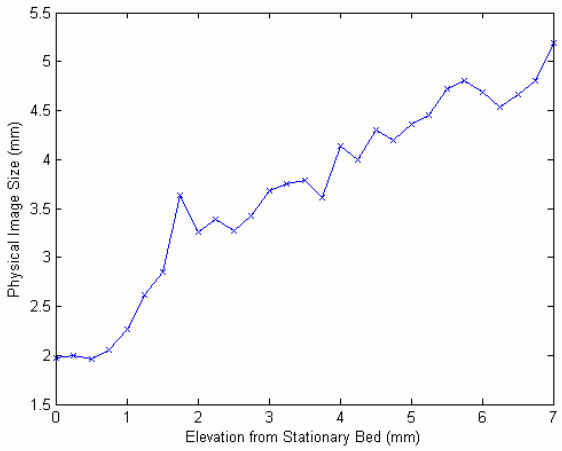

Figure 5.16 Physical Image Size, Variance of Intensity

5.4.4.4 Discussion of Methods

Three dynamic calibration methods have been developed to convert pixel displacements to physical displacements. The application of an accurate calibration is critical to the boroscope technique and the three methods (intensity matching, maximum intensity and variance of intensity) represent three different approaches to calibration.

The intensity matching method is the most simplistic. The method looks only at the initial region before the cone of light fully enters the imaging window. It assumes that in this region, the moving calibration and the sheet flow layer data should be the same. Yet even in this region the moving calibration and sheet flow layer can be very different. Particles in the moving calibration are at a fixed distance from both the imaging window and the light delivery window. Although this is considered to be a highly concentrated region of the sheet flow, it cannot necessarily be said that particles are at a fixed distance from both windows in the real data. This could limit

the amount of light entering the image, which can be seen in the factor of ~2 discrepancy between the maximum intensity values. If a lesser amount of light is permitted to enter the image in the sheet flow data as opposed to the moving calibration data, this could underestimate the window size in the intensity matching method. This method can be considered a lower bound.

The maximum intensity method can also be skewed. Although the normalization should help, especially in the highly-concentrated initial region, three-dimensional effects make the maximum intensity method less reliable in less concentrated regions. In the moving calibration, particles are always at a fixed, known distance from the scope tip. In the sheet flow layer, especially in the less concentrated areas, it is possible for the scope to image particles that are both right next to the imaging window and several grain diameters from the imaging window. The maximum intensity in the image will be high due to the close particle. Likewise, there is a possibility in less concentrated areas to record images with no particles, causing the maximum intensity in the image to be low. Due to this wide variability in maximum intensity, this method should be considered an upper bound.

The variance of intensity method represents an improvement on the other two methods. While the intensity matching method is limited based on light and the maximum intensity method can be skewed based on particle location, the variance of intensity is more robust because it represents a ratio rather than a fixed value. The ratio of light regions to dark regions should decrease as the sediment concentration decreases. This ratio will decrease as the scope moves into less concentrated regions in the sheet flow layer. This ratio will also decrease as the scope gets farther away from the sediment in the moving calibration. For this thesis, the variance of intensity method will be considered the most ideal calibration.

5.4.5 Use of In-Situ Calibration

Although the in-situ calibration should not be used for the entire sheet flow layer, it can be used to modify the variance of intensity method. The maximum intensity and variance of intensity values are calculated for the last four in-situ calibration trials. The resulting median values of the maximum intensity and the variance of intensity are 46 counts and 21.7 counts^2, respectively. Using the moving calibration data, these values correspond to physical image sizes of 3.01 and 2.80 mm, respectively. Applying the MQD routine to the in-situ calibration resulted in a physical image size of 2.10 mm. Using the image size found from the in-situ calibration closes the gap between the calibration data and the sheet flow layer data. This results in conversion factors for the maximum intensity method and the variance of intensity method of 0.70 and 0.75, respectively. Figures 5.17 and 5.18 show these conversions applied to the curves of the physical image size, to create the final calibration curves for the sheet flow layer data.

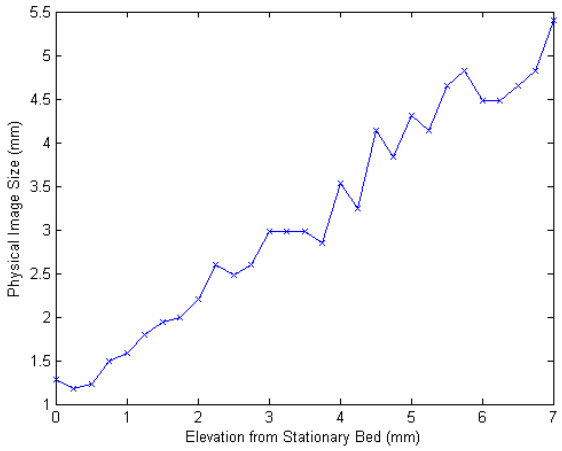

Figure 5.17 Normalized Image Size, Maximum Intensity

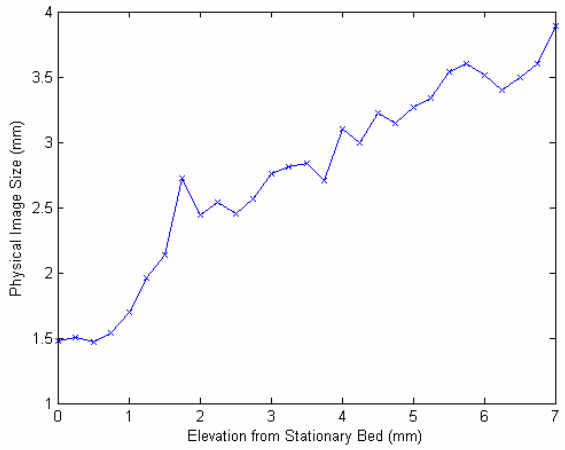

Figure 5.18 Normalized Image Size, Variance of Intensity

5.5 Sheet Flow Layer Data

Images are taken throughout the entire sheet layer. The scope is initially positioned in the non-moving sediment bed. This is accomplished by manually adjusting the vertical position of the scope until images visually show no movement. From this non-moving position, the scope is driven up through the bed at 0.25 mm intervals using the vertical positioning system. Image pairs are collected for 9 minutes at each location, at a rate of 10 Hz pairs. Time between images (Δt) is set at 0.1 ms for each location. The nine-minute data set at 10 Hz pairs totals 10,800 images per point, which are recorded in 1,200 image sections to ease post-processing. The data acquisition system occasionally locks up during image collection, at which point the data point is either re-taken or the record is determined long enough.

The 9-min data record is determined from several factors. A 9-minute sample develops convergence of the mean PIV-determined displacements. Since images require significant memory, 9-min samples limit the amount of storage as well as the amount of post-processing required. Figure 5.19 shows the cumulative mean of the

streamwise velocity at an elevation of 3 mm, which is within the sheet flow layer. The percentage difference of the cumulative mean from the global mean is also shown, which decreases to less than 5%.

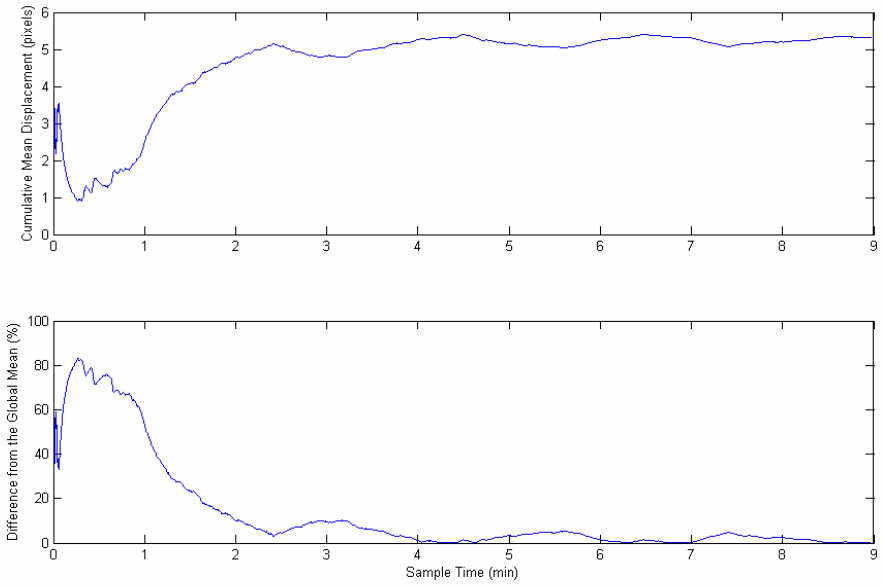

Figure 5.19 Displacement Calculation Stability

Image data is collected at 0.25 mm intervals moving vertically up through the sheet flow layer. Image 5.4 shows typical, unfiltered images from the boroscope at 1 mm increments. At the 0 mm elevation, images appear dark because the sediment grains are packed so tightly that light from the illumination window is blocked from reaching the imaging window. Light in the image increases with increasing elevation until it reaches a maximum intensity at the 3 mm elevation. Light intensity decreases with increasing elevation above this point as the sediment concentration decreases. With a decrease in sediment concentration, there are fewer particles in the flow to reflect the light back onto the imaging window.

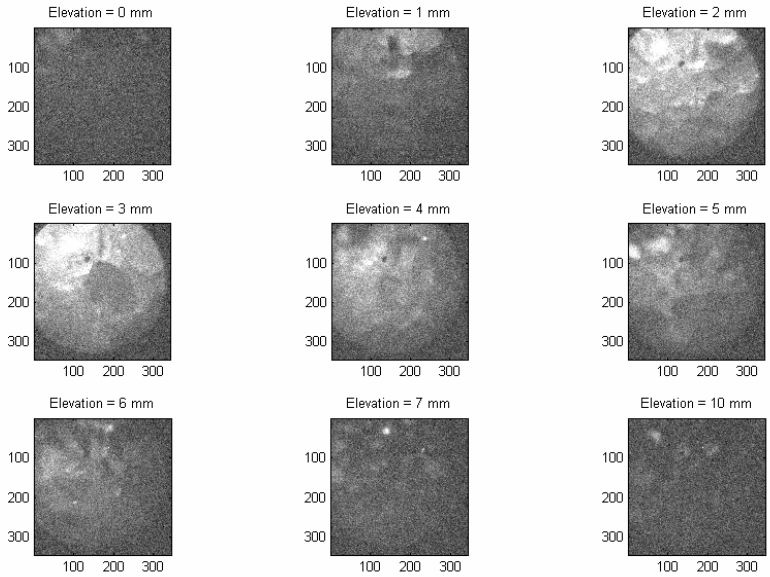

Image 5.4 Typical Boroscope Images

The changing light conditions associated with the changing sediment concentrations causes difficulties in accurately determining sediment displacements. These difficulties are seen in the histograms of determined pixel displacements, as shown in Figure 5.20 for the same elevations as the typical images shown in Image 5.3. The pixel displacements are filtered using an adaptive Gaussian filter with a three sigma range to remove extraneous displacements. It is obvious from the histograms that an adaptive Gaussian filter does not completely smooth the data. At higher elevations, displacements of zero still exist not as extraneous data points but as real data calculated from the MQD routines at times where no particles appear in the image pair. This is real data and should be examined more closely in the future. For this study, the mean filtered displacements were used with the realization that this technique is being initially developed. In future development of this technique, sources of error such as this should be more carefully examined.

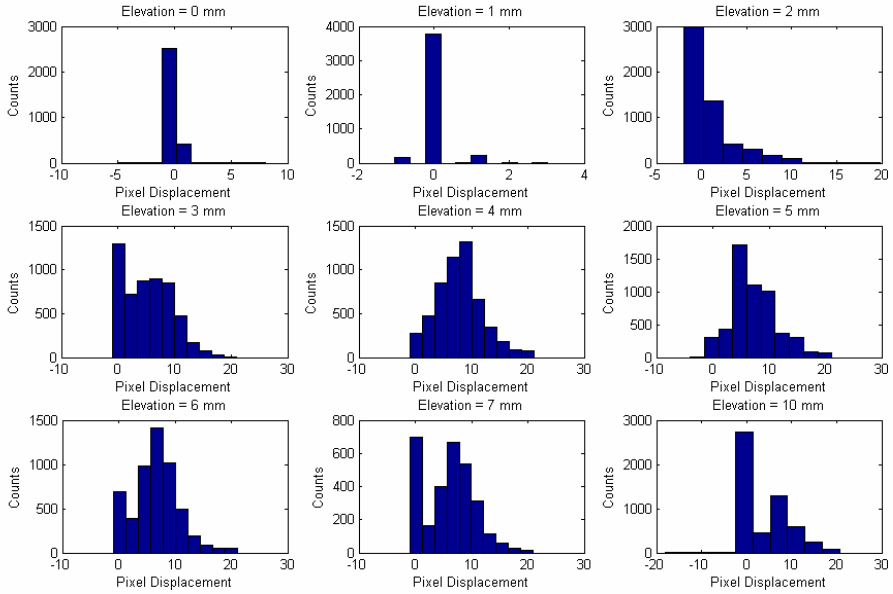

Figure 5.20 Streamwise Pixel Displacement Histograms

The mean pixel displacements in the streamwise direction are shown in Figure 5.21 along with the 95% confidence interval calculated by the bootstrap method.

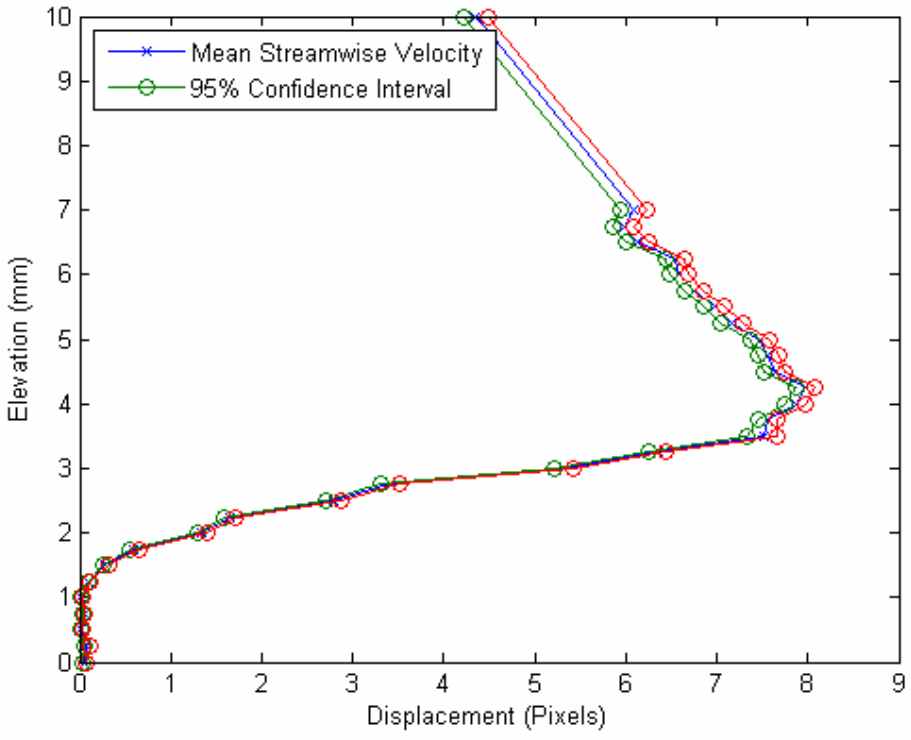

Figure 5.21 Streamwise Pixel Displacement

Physical velocity units are applied to the streamwise pixel displacements using the three different calibration methods discussed previously using the following relationship:

$$U = \frac{\Theta}{344 Pixels} * \frac{1}{\Delta t} * \omega$$

where ω = pixel displacement determined from the MQD routine.

The average streamwise sediment velocity sheet flow layer profiles for all three calibration methods are shown in Figure 5.22.

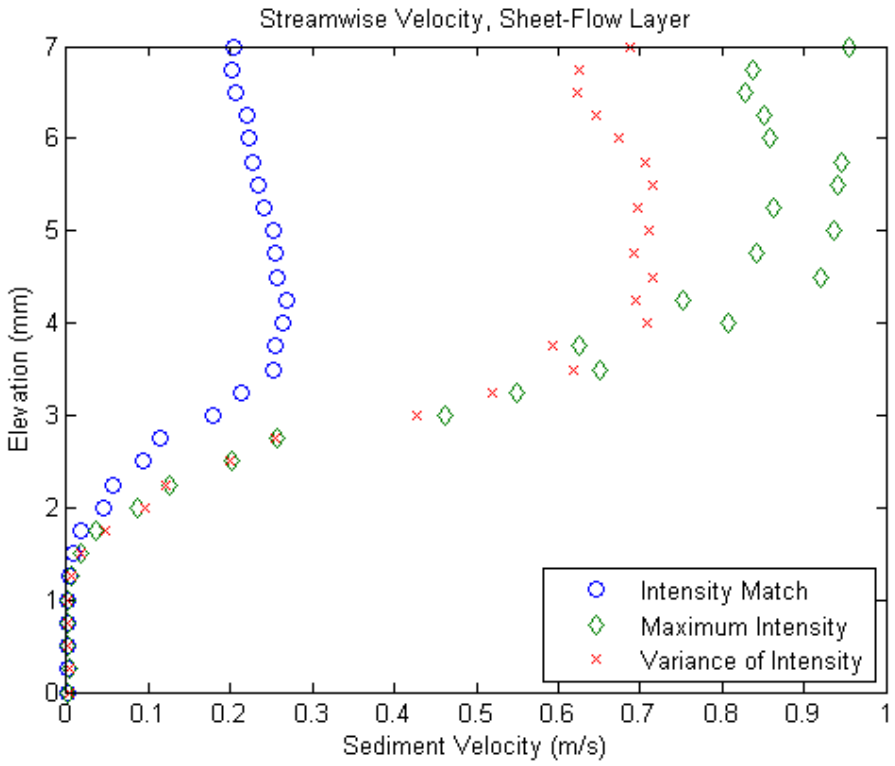

Figure 5.22 Streamwise Physical Velocities

Similarly, vertical pixel displacements (Figure 5.23) are filtered with the adaptive Gaussian filter and converted to physical units using the three calibration methods (Figure 5.24). The MQD routines are optimized to minimize the search window and reduce the computation time. The displacement value at 3.5 mm contains several vectors outside the search radius which skew the result at that location. This applies to the vertical displacements only, and only at this one location, so it can be effectively discarded.

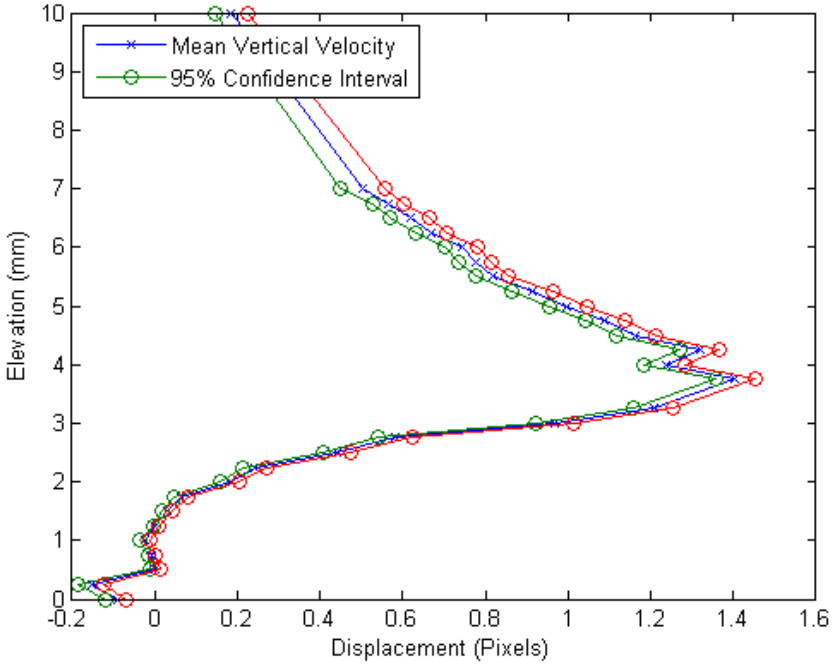

Figure 5.23 Vertical Pixel Displacements

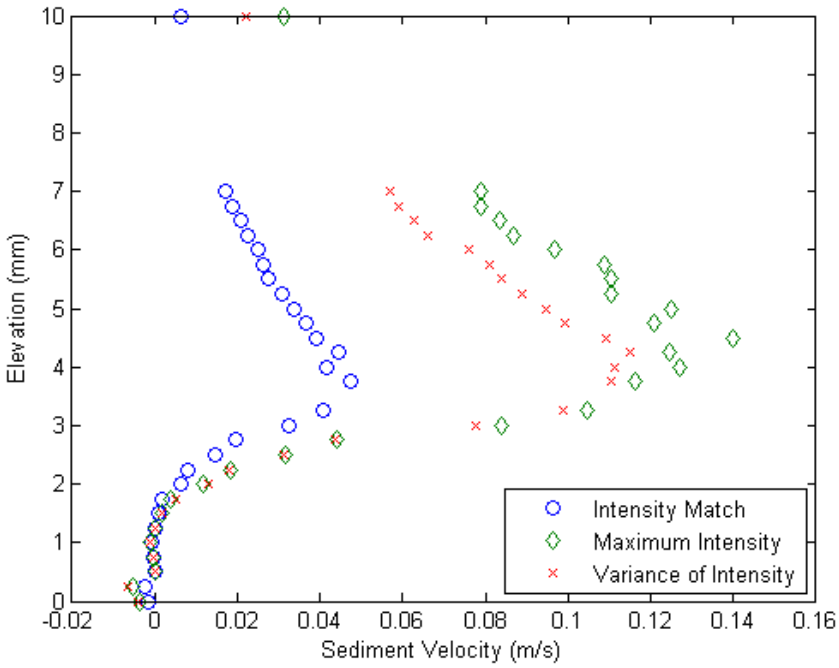

Figure 5.24 Vertical Physical Velocities

As expected, the intensity match calibration seems to underestimate both streamwise and vertical velocities. Although the maximum intensity does result in the highest velocities, as expected, it is interesting to note that velocities determined using the variance of intensity calibration agree with velocities determined using the maximum intensity calibration up to an elevation of nearly 3.5 mm. Velocity verification using separate calibration techniques helps to establish the ability of the calibrations to determine accurate velocity measurements, at least in the highly concentrated region of flow.

While the agreement between the two calibration techniques verifies the calibrations in the highly concentrated region, the decreasing velocities in the higher, less dense regions display the need for additional calibration methods. The intensity match method and the variance of intensity method both show an obvious decrease in streamwise velocity with elevation. It seems the maximum intensity method also shows a velocity decrease with elevation, although not as significant as the other two techniques. This might suggest the maximum intensity method is better suited to handle a wider range of sediment concentrations. Future research should focus on further development of these calibration techniques as well as the search for additional parameters that might solidify these calibration techniques.

CHAPTER 6

CONCLUSION

Two separate measurement techniques are used to measure sediment velocities throughout the entire water column. A well-studied technique, acoustic Doppler velocimetry, is used to measure velocities in the suspended region while a new technique, the boroscope, is used to measure velocities in the highly concentrated sheet layer. Two techniques are necessary to capture the entire column, as the ADV is unable to accurately resolve velocities within the sheet layer due to blocking effects and the boroscope is unable to resolve velocities in the suspended region due to calibration difficulties.

The location of the fixed bed is easily determined using the boroscope data. The calibrated streamwise velocities remain at 0 m/s until 1 mm above the initial measurement location. Visual observations of the image data confirm the absence of sediment movement until the 1 mm boroscope measurement location. This location is used as the fixed bed, zero elevation. Boroscope data is considered valid until 2 mm above the fixed bed elevation. The two calibration techniques (variance of intensity and maximum intensity) produce good agreement up to this elevation and a visual inspection of the image data above this location shows a decrease in the dense concentration needed for accurate velocity determination. Boroscope data through the sheet produces velocities ranging from 0 m/s to approximately 0.4 m/s. ADV data is considered valid starting at a velocity of 0.385 m/s and is placed at the boroscope elevation that corresponds to this velocity, as found by linearly interpolating the boroscope velocities. The entire velocity profile, from the fixed bed location to the free stream, is shown below in the following four figures.

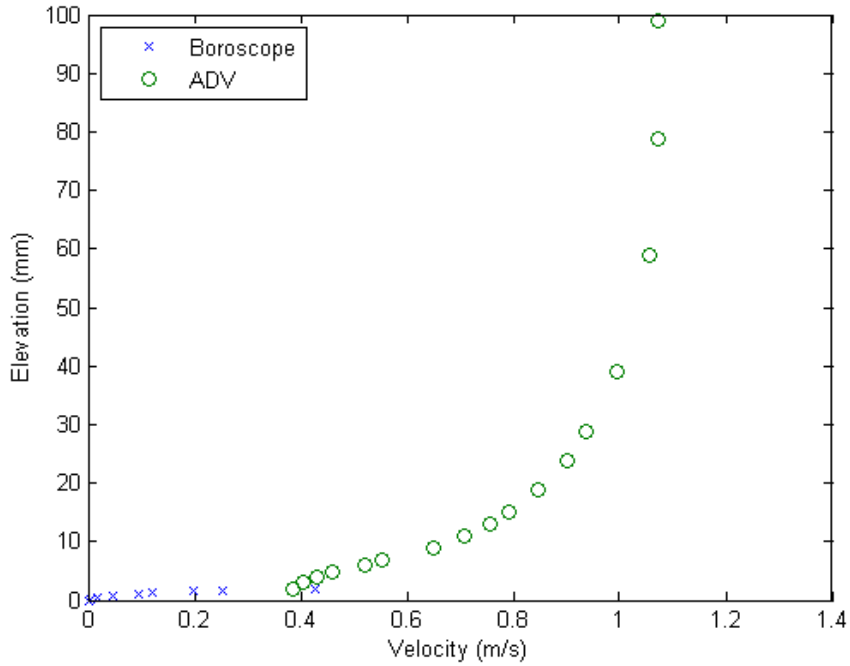

Figure 6.1 Joint Profile, Boroscope and ADV Sheet Flow Data

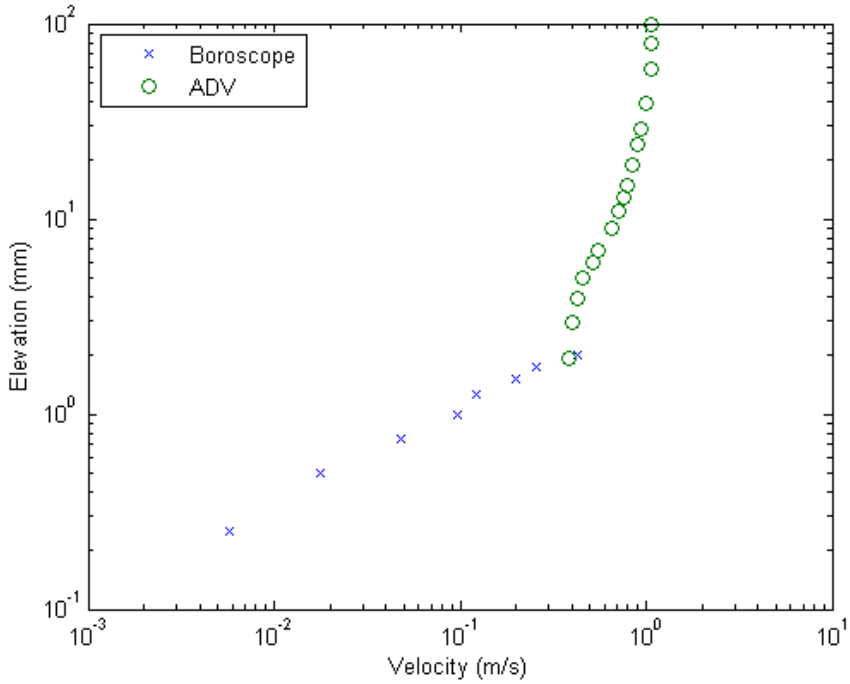

Figure 6.2 Joint Profile, Boroscope and ADV Sheet Flow Data (logarithmically plotted)

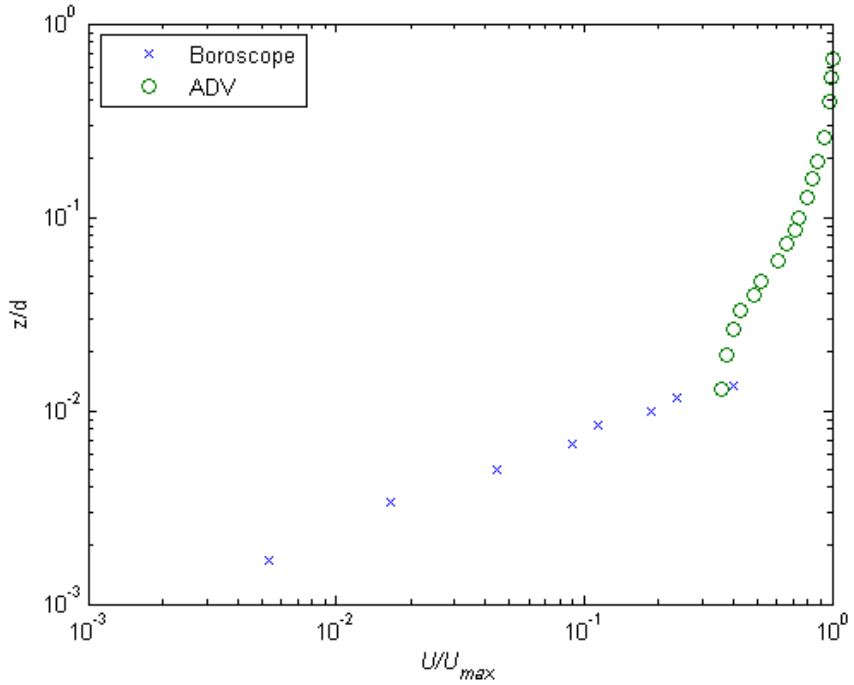

Figure 6.3 Joint Profile, Normalized by Maximum Velocity and Water Depth

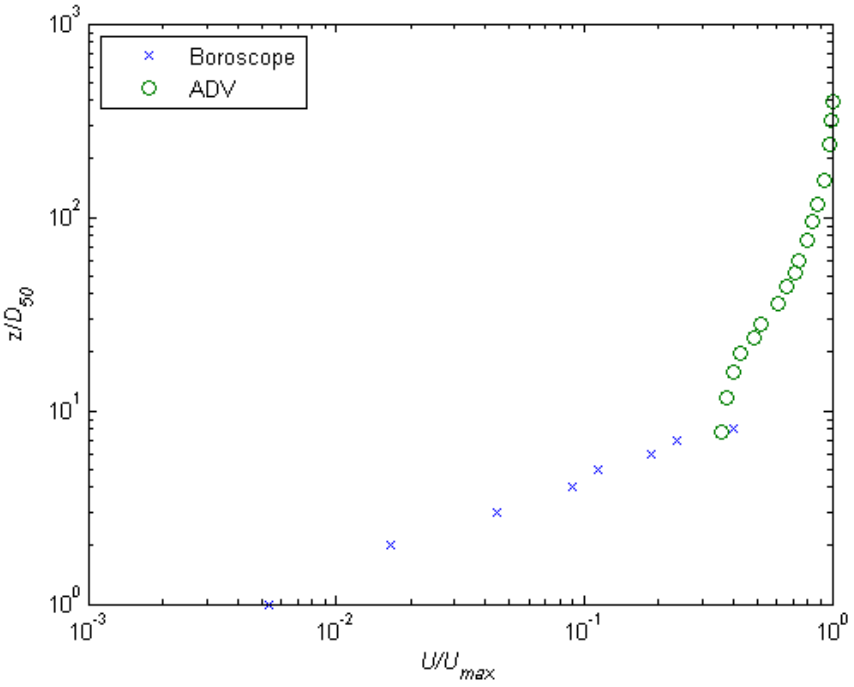

Figure 6.4 Joint Profile, Normalized by Maximum Velocity and Median Grain Diameter

The boroscope data and ADV data merge to create a continuous profile. The transition between the two techniques is not seamless, most likely because of the limitations of the two techniques. Still, the suspended profile agrees with previous studies and the sheet flow profile adheres to a power law similar to what was found by Sumer et al. (1996) according to the form:

$$\frac{\bar{u}}{U_*} = b\left(\frac{z}{d_{50}}\right)^n$$

where $\bar{u}$ = average sediment velocity, U_* = bed friction velocity (0.0447 m/s found previously), z = elevation above the fixed bed, d_{50} = median grain diameter of 0.25 mm. The power fit results in *b* and *n* values of 0.0524 and 2.479 respectively and is shown in Figure 6.4. This is significantly different than the respective *b* and *n* values of 4.24 and 0.75 found by Sumer et al. These differences can most likely be attributed to the particle sizes used by Sumer et al., which were approximately ten times as large as the natural sand used in this study, as well as the measurement technique employed by Sumer et al., the use of a Pitot-tube with an opening on the order of the grain sizes studied.

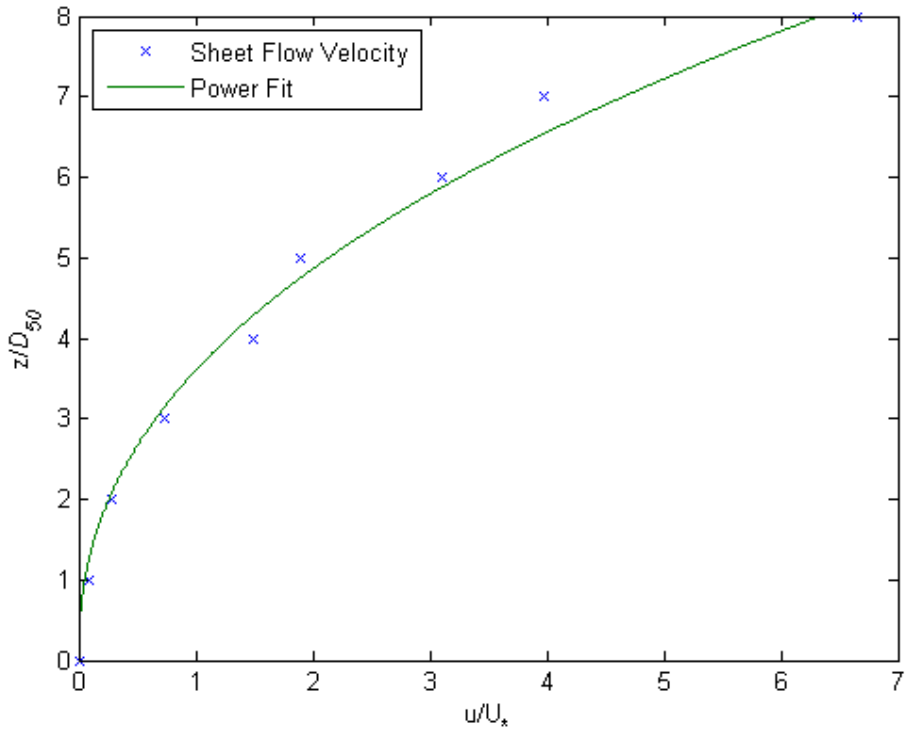

Figure 6.5 Sheet Layer Sediment Velocities and Power Fit Curve

The attempt to compare boroscope data with experiments completed by Sumer et al. highlight the difficulties associated with developing a new technique and the capture of data that has been difficult, if not impossible, to measure. If there was established experimental data available to verify this technique, the technique itself would be irrelevant.

While direct verification of the boroscope sheet layer data is not available, additional experiments could greatly help establish the validity of the technique. It is recommended that future experimental work should include an investigation of the flume characteristics of clean water flows under sheet flow conditions. Both time and logistics prevented the author from examining the flume characteristics of clean water flows in more depth. Also, the calibrations developed in this study are relevant only

for the first few millimeters above the fixed bed, where the sediment concentration is the greatest. This is not to say the boroscope does not have the capability of imaging particles in less dense regions, there simply needs to be a calibration which distinguishes the physical scale of the imaging window. Future boroscope generations should be designed to address this issue and additional metrics should be considered to develop a calibration that is valid for a wide range of particle concentrations. Also, the capture of sediment concentrations concurrently with sediment velocities would provide invaluable information both for the further development of the boroscope and for the sediment transport research community. This could be accomplished by utilizing concentration measurement techniques (such as the previously mentioned CCM probes) along with the boroscope or by developing a technique to determine sediment concentrations from the boroscope images. Sediment concentrations could be determined through quantification of image intensity values. Image intensity values or variations in intensity values could potentially be correlated to sediment concentrations. This would require an extensive calibration technique on the scale of the one developed in this thesis for sediment velocities. It is not unreasonable to think a calibration facility could be built that would allow calibration of boroscope images against known sediment concentrations. The capture of sediment concentration and velocity allows for comparison to published experiments on sheet-layer concentrations as well as the ability to capture sediment flux measurements within the highly concentrated sheet-layer.

This study lays the groundwork for a very promising and exciting measurement technique. With additional development, this technique could be used to measure flows that have previously been impossible to capture due to scale or particle density issues. Yet the value of this study doesn't simply lie in the future work that it creates. The techniques developed to measure sediment velocities throughout the

entire water column, from the fixed bed to the free stream, provide a complete picture of unidirectional sheet flow sediment transport that has not been seen before. Specifically, the ability to capture sediment velocities in the swash zone which have been previously unobtainable provides much needed insight into a very complex and wide-reaching problem. This boroscopic measurement technique provides the experimental data necessary to advance the understanding of swash zone hydrodynamics and sediment transport in general.

BIBLIOGRAPHY

Bennett, S. J., J. S. Bridge and J.L. Best (1998). "Fluid and sediment dynamics of upper stage plane beds." Journal of Geophysical Research-Oceans **103**(C1): 1239-1274.

Campbell, L., I. McEwan, V. Nikora, D. Pokrajac, M. Gallagher and C. Manes (2005). "Bed-load effects on hydrodynamics of rough-bed open-channel flows." Journal of Hydraulic Engineering-ASCE **131**(7): 576-585.

Carlowicz, M. (2004). Breaking Waves and Shifting Sands. Woods Hole Currents. **10:** 4-9.

Cowen, E. A. and S. G. Monismith (1997). "A hybrid digital particle tracking velocimetry technique." Experiments in Fluids **22**(3): 199-211.

Dick, J. E. and J. F. A. Sleath (1991). "Velocities and Concentrations in Oscillatory Flow over Beds of Sediment." Journal of Fluid Mechanics **233**: 165-196.

Dohmen-Janssen, C. M. and D. M. Hanes (2002). "Sheet flow dynamics under monochromatic nonbreaking waves." Journal of Geophysical Research-Oceans **107**(C10): 3149.

Elfrink, B. and T. Baldock (2002). "Hydrodynamics and sediment transport in the swash zone: a review and perspectives." Coastal Engineering **45**(3-4): 149-167.

Grue, J., P. L-F Liu and G. K. Pedersen (Editors) (2004). PIV and Water Waves. World Scientific Publishing Co., 1-50.

Gui, L. and W. Merzkirch (2000). "A comparative study of the MQD method and several correlation-based PIV evaluation algorithms." Experiments in Fluids **28**(1): 36-44.

Hassan, W. N. and J. S. Ribberink (2005). "Transport processes of uniform and mixed sands in oscillatory sheet flow." Coastal Engineering **52**(9): 745-770.

Helmle, C. S. (2005). A Quantitative Thermal Imaging Technique to Extract a Cross-stream Surface Velocity Profile From a Flowing Body of Water. Department of Civil and Environmental Engineering. Ithaca, Cornell University. **Master of Science:** 67.

Horikawa, K., A. Watanabe and S. Katori (1982). "Sediment transport under sheet flow conditions." Proceedings of the 18th International Conference on Coastal Engineering-ASCE: 1335-1352.

Jenkins, J. T. and D. M. Hanes (1998). "Collisional sheet flows of sediment driven by a turbulent fluid." Journal of Fluid Mechanics **370**: 29-52.

Kaftori, D., G. Hetsroni, and S. Bannerjee. (1995). "Particle Behavior in the Turbulent Boundary-Layer .1. Motion, Deposition, and Entrainment." Physics of Fluids **7**(5): 1095-1106.

Kaftori, D., G. Hetsroni, and S. Banerjee (1995). "Particle Behavior in the Turbulent Boundary-Layer .2. Velocity and Distribution Profiles." Physics of Fluids **7**(5): 1107-1121.

Kennedy, J. F. (1969). "The Formation of Sediment Ripples, Dunes, and Antidunes." Annu. Rev. Fluid. Mech. **1**: 147-168.

Leatherman, S. P., Douglas, B. C., and LaBrecque, J. L. (2003). Sea Level and Coastal Erosion Require Large-scale Monitoring. EOS. **84:** 13 and 16.

Lyn, D. A. (1986). Turbulence and Turbulent Transport in Sediment-laden Open-channel Flows. W. M. Keck Laboratory of Hydraulics and Water Resources, Division of Engineering and Applied Science. Pasadena, California Institute of Technology. **Doctor of Philosophy:** 244.

McLean, S. R., J. S. Ribberink, C. M. Dohmen-Janssen and W. N. Hassan (2001). "Sand transport in oscillatory sheet flow with mean current." Journal of Waterway Port Coastal and Ocean Engineering-ASCE **127**(3): 141-151.

Muste, M., V. C. Patel and R. N. Parthasarathy (1996). "Discriminator laser Doppler velocimetry for measurement of liquid and particle velocities in sediment-laden flows." Experiments in Fluids **22**(1): 45-56.

Muste, M. and V. C. Patel (1997). "Velocity profiles for particles and liquid in open-channel flow with suspended sediment." Journal of Hydraulic Engineering-ASCE **123**(9): 742-751.

O'Donoghue, T. and S. Wright (2004). "Concentrations in oscillatory sheet flow for well sorted and graded sands." Coastal Engineering **50**(3): 117-138.

O'Donoghue, T. and S. Wright (2004). "Flow tunnel measurements of velocities and sand flux in oscillatory sheet flow for well-sorted and graded sands." Coastal Engineering **51**(11-12): 1163-1184.

Ribberink, J. S. and A. A. Alsalem (1995). "Sheet Flow and Suspension of Sand in Oscillatory Boundary-Layers." Coastal Engineering **25**(3-4): 205-225.

Sumer, B. M., L. H. C. Chua, N. S. Cheng and J. Fredsøe (2003). "Influence of turbulence on bed load sediment transport." Journal of Hydraulic Engineering-ASCE **129**(8): 585-596.

Sumer, B. M., A. Kozakiewicz, J. Fredsøe and R. Deigaard (1996). "Velocity and concentration profiles in sheet-flow layer of movable bed." Journal of Hydraulic Engineering-ASCE **122**(10): 549-558.